Technical Report

TR-01-25

Nuclear Waste Containment Materials

Papers related to the SKB waste disposal programme presented at the Materials Research Society Spring Meeting, April 19, 2001

Svensk Kärnbränslehantering AB

August 2001

Svensk Kärnbränslehantering AB
Swedish Nuclear Fuel
and Waste Management Co
Box 5864
SE-102 40 Stockholm Sweden
Tel 08-459 84 00
+46 8 459 84 00
Fax 08-661 57 19
+46 8 661 57 19

Nuclear Waste Containment Materials

Papers related to the SKB waste disposal programme presented at the Materials Research Society Spring Meeting, April 19, 2001

Svensk Kärnbränslehantering AB

August 2001

Contents

Native Copper in Permian Mudstones from South Devon: A Natural Analogue of Copper Canisters for High-Level Radioactive Waste

Antoni E. Milodowski[1], Michael T. Styles[1], Lars Werme[2] and Virginia M. Oversby[3]
[1]British Geological Survey, Kingsley Dunham Centre,
Keyworth, Nottingham, NG12 5GG,United Kingdom
[2]Svensk Kärnbränslehantering AB (SKB),
Box 5864, SE-102 40, Stockholm, Sweden
[3]VMO Konsult,
Karlavägen 70, S-114 59, Stockholm, Sweden

ABSTRACT

Native copper (>99.9% Cu) sheets associated with complex uraniferous and vanadiferous concretions in Upper Permian mudstones from south Devon (United Kingdom) have been studied as a "natural analogue" for copper canisters designed to be used in the isolation of spent fuel and high-level radioactive wastes (HLW) for deep geological disposal. Detailed analysis demonstrates that the copper formed before the mudstones were compacted. The copper displays complex corrosion and alteration. The earliest alteration was to copper oxides, followed sequentially by the formation of copper arsenides, nickel arsenide and copper sulphide, and finally nickel arsenide accompanied by nickel-copper arsenide, copper arsenide and uranium silicates. Petrographic observations demonstrate that these alteration products also formed prior to compaction. Consideration of the published history for the region indicates that maximum compaction of the rocks will have occurred by at least the Lower Jurassic (i.e. over 176 Ma ago). Since that time the copper sheets have remained isolated by the compacted mudstones and were unaffected by further corrosion until uplift and exposure to present-day surface weathering.

INTRODUCTION

The use of copper canisters for spent fuel disposal

The Swedish Nuclear Fuel and Waste Management Company (SKB) plan to dispose of HLW encased in a steel inner container within an outer canister of copper [1]. The canisters will be surrounded by compacted bentonite buffer within a repository constructed in granitic host rocks at a depth of 700 m. [1]. SKB has set a performance requirement that the copper canister should isolate the waste for at least 10^5 years until the various radioactive components decay to acceptable levels [1]. Neither the canister nor its corrosion products must have a deleterious on other barrier components (backfill and host rock) in order that they remain effective in attenuating radionuclide migration in the event of canister failure.

Copper has been identified in several international waste disposal programmes as a suitable canister material on the basis of its cost and corrosion resistance [1,2,3]. Experimental and theoretical studies demonstrate a wide stability range for metallic copper, and suggest that corrosion effects will be small in the mildly alkaline and reducing environment anticipated for a potential repository site [1]. However, the potential presence of dissolved sulphides in groundwater, or the formation of sulphides through the activity of sulphate-reducing bacteria

may compromise the long-term stability of the copper. This could significantly enhance copper corrosion. Current SKB design concepts consider that both of these factors will be minimal [1]. However, groundwater chemistry may vary significantly, in response to climatic changes (e,g, glaciation and sea level change) on a timescale relevant to PA [4]. The complex interplay of different processes occurring over these long periods of time may not be adequately modelled or reproduced in short-term laboratory experiments. Uncertainties in the long-term predictions of repository performance can be reduced by studying the analogous processes in natural systems ("natural analogues") that have operated over geological timescales [5].

Previous analogue studies of copper stability

Previous analogue investigations on the corrosion and longevity of copper have focussed largely on the study of buried archaeological or industrial artefacts composed of copper or tin-bronzes [5,6,7]. However, these are not truly representative of repository materials and environments [5]. A detailed investigation was made of the corrosion of a bronze cannon recovered from the wreck of the Swedish man-of- war "Kronan", which sank in the Baltic Sea during the Battle of Öland in 1676 [3,5,8]. The cannon was buried vertically in tightly-packed, seawater-saturated smectitic clay sediment. It presented the opportunity to study corrosion effects across a redox profile through the sediments, which provides some information that might be broadly analogous to a copper canister enclosed in bentonite. However, the geochemical environment of the Kronan Cannon is considered to be more oxidising than that anticipated within a HLW repository [5].

Whilst buried industrial and archaeological artefacts provide valuable information on processes over the 10 to 10^3 year timescale, observations from geological analogues are also required to examine processes and to validate model predictions over the longer timescales required for PA. Very few geological analogues for copper corrosion have been studied in detail. Marcos [9] undertook a natural analogue study of native copper from several geological associations and found the metal remained stable over a broad range of hydrogeological environments. However, none of these environments were really applicable to repository conditions.

THE LITTLEHAM MUDSTONE FORMATION NATURAL ANALOGUE SITE

Geological background

The geology of the site is detailed elsewhere [10] but a brief summary is given here. The occurrence of rare native copper from Littleham Cove (south Devon), on the southwest coast of England, was originally recorded by Harrison [11]. It occurs in thin sheets associated with diagenetic concretions (containing high concentrations of uranium, vanadium and other metals with arsenic) hosted by mudstones and siltstones of the Upper Permian (230-250 Ma) Littleham Mudstone Formation. These rocks are exposed in the sea cliffs and beach at Littleham Cove - between Budleigh Salterton and the River Exe, where they are overlain directly by Triassic strata (figure 1). They consist mainly of continental ("red bed") mudstones and siltstones (representing

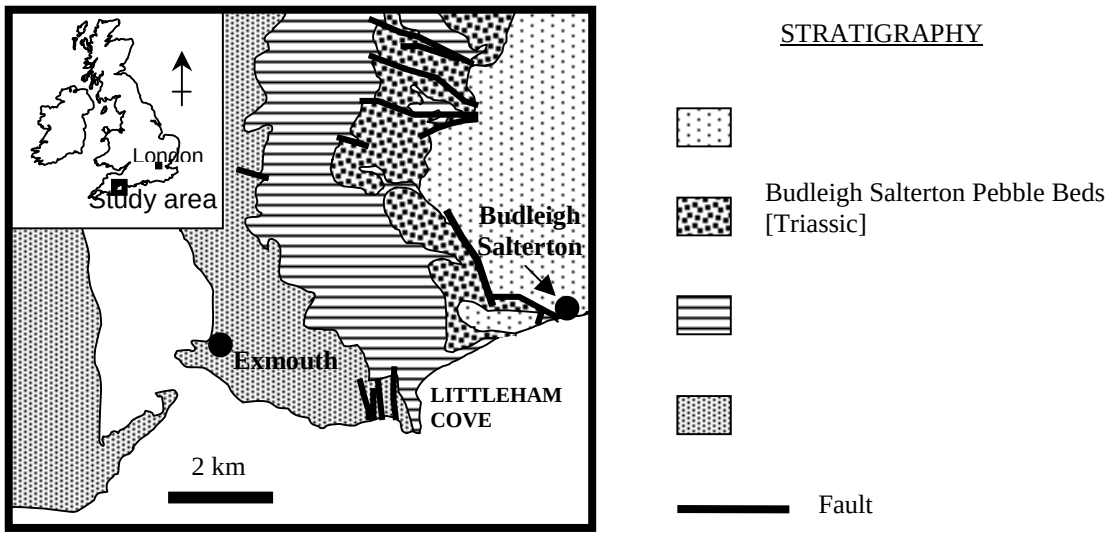

Figure 1. Location map and simplified geology of the Littleham Cove site.

overbank flood deposits, levee and crevasse splay deposits, and ephemeral lake deposits) and minor thin channel and sheet flood sandstones. These were laid down within an alluvial floodplain or flood basin near the western margin of the Wessex Basin. This complex basin developed across much of central southern England (and adjacent offshore areas) from the Permian to the Tertiary and is filled by thick sequences of Mesozoic and Tertiary strata [12].

The concretions have nucleated within pale green reduction spots developed within the red-brown ferruginous mudstone and siltstone matrix, and vary in morphology from simple spheres to complex and stellate forms [11]. Earlier studies, on these and similar feature elsewhere, suggested that the reduction spots formed locally around detrital organic fragments during burial diagenesis [see 10]. Reduction is also seen along more permeable sandy laminae, sand-filled desiccation cracks in the mudstone, and along fractures associated with small faults - implying that reducing pore fluids also permeated through the strata.

Analytical details

Archived materials at the British Geological Survey [11] were re-examined together with new material collected from the site [10]. Five copper-bearing concretions were examined in detail as polished sections. They were initially examined under a petrological microscope in reflected light. More detailed petrological observations were made by backscattered scanning electron microscopy (BSEM), using an energy-dispersive X-ray microanalysis (EDXA) to aid mineral identification. Quantitative microchemical data and X-ray maps of elemental distribution were obtained by wavelength-dispersive electron probe microanalysis (EPMA). The bulk rock and clay mineralogy of the host rocks were determined by X-ray diffraction analysis (XRD). Full analytical details are given elsewhere [10].

Petrological observations

The red-brown mudstone and siltstone host rocks are composed mainly of detrital quartz sand and silt with a clay matrix dominated by major illite. Some beds contain smectite as the

major clay mineral. Other minor to trace detrital components include detrital K-feldspar, plagioclase, chloritized mica and iron-titanium oxides. Finely disseminated iron and titanium oxide (probably largely authigenic hematite and anatase) are present throughout the matrix, which is sometimes cemented by calcite. Green reduction spots in the mudstones have an altered mineralogy, in which fine framboidal pyrite is formed at the expense of hematite, and chlorite is formed at the expense of smectite (in the case of smectitic host rock).

Native copper (>99.9% Cu), containing small inclusions of silver (>99.9% Ag), occurs within the concretions as thin discoidal plates (figure 2a) up to 160 x 90 mm in diameter, and up to 4 mm thick. Each plate is a composite of several stacked thin sheets of copper, which vary in thickness from <0.1 to 2 mm (e.g. figure 2b). The copper sheets have grown along, or sub-parallel to, thin siltstone bedding laminae in the mudstones, and along microfractures cutting the same bedding laminae. Inclusions of corroded quartz sand grains and relicts of cross-fibre calcite veining indicate that the sheets grew by replacement of clastic material

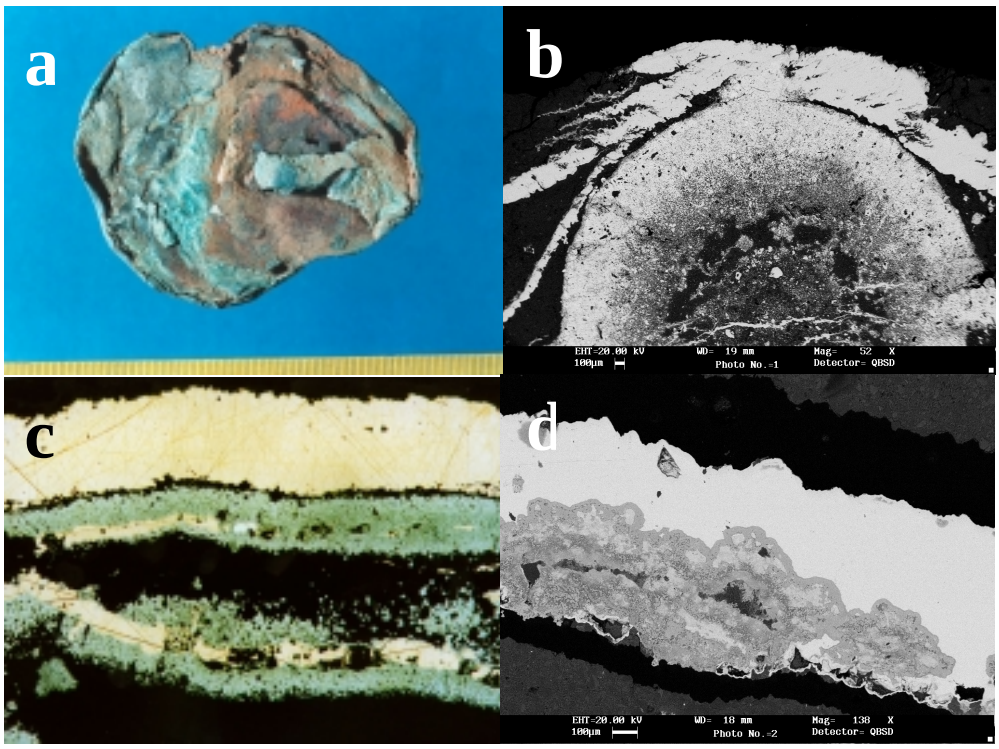

Figure 2. [a] Typical native copper plate with residual light grey clay matrix still attached (field of view is 12 mm wide). [b] BSEM image showing compactional deformation of copper sheets (bright) around a spherical banded concretion of nickel arsenide (bright) enclosing a core of vanadian illite (dark) containing bright grains and thin sheets of native copper (bright). [c] Reflected light photomicrograph showing asymmetric alteration of copper sheet to nickel arsenide (field of view is 2.6 mm wide). [d] BSEM image showing alteration of copper sheet to cuprite (dull grey), overlain by a thin fringe of nickel and copper arsenides (bright).

along coarser sandy laminae pre-existing bedding-parallel microfractures. This reflects mineral deposition from fluids moving along the more permeable pathways in the mudstone. Fine disseminated grains (5-100 µm) and very thin sheets of copper also occur within the cores

of complex uraniferous-vanadiferous concretions. These concretions comprise cores of vanadian illite or roscoelite ($KV_2AlSi_3O_{10}[OH]_2$) intergrown with montroseite (VO·OH), surrounded by haloes of nickel arsenides (including maucherite, Ni_3As_2; niccolite, NiAs; and rammelsbergite, $NiAs_2$). Minor amounts of copper, copper-nickel and nickel-cobalt arsenides (e.g. algodonite, Cu_6As; and chalcocite, Cu_2S), pyrite and uranium silicate (probably coffinite, $U[SiO_4]_{1-x}[OH]_{4x}$), together with traces of fine grained galena (PbS)and clausthalite (PbSe) are intergrown with the nickel arsenides. Trace amounts of fine grained gold and gold-copper alloys are also present in the matrix and nodules.

The copper sheets display compactional deformation around the more competent concretions (figure 2c), indicating that both grew very early during sediment diagenesis before any significant burial compaction of the strata. There is a close paragenetic relationship between copper and nodule development. The inclusion of thin copper sheets and fine copper inclusions in the cores of the nodules indicates that copper deposition started before concretion growth. However, copper sheets external to concretions are thicker, suggesting that copper growth continued during and/or after concretion growth.

The copper displays complex corrosion and alteration. Often this affects the sheets asymmetrically, with alteration on one side of the sheet whilst the opposite surface is unaffected (figure 2b and d). In a composite stack of several thin sheets, the corrosion is commonly on the same surface in each successive sheet. The reason for this characteristic corrosion is not yet clear. The earliest formed alteration product is copper oxide (principally cuprite, Cu_2O with minor tenorite, CuO). The cuprite forms colloform corrosion layers that "eat" into the copper metal (figure 2d). This was followed by the formation of copper arsenides (including algodonite and unidentified minerals). These are closely associated with the dissolution of native silver inclusions in the copper, and form fringes on the cuprite and copper surfaces. The copper arsenide alteration was followed by the deposition of extensive rims of dull-grey nickel arsenide similar to maucherite in composition, accompanied by minor chalcocite. Thin alteration fringes of bright nickel arsenides (including niccolite), and sometimes accompanied by copper arsenide, copper-nickel arsenide and uranium silicate form later alteration layers. A similar sequence of mineral deposition is seen in the growth of the associated uraniferous-vanadaiferous concretions, indicating a close temporal relationship between the two features. Where the copper has been exposed to surface weathering, thin films of secondary copper sulphates, carbonate and chloride minerals are formed.

CONCLUSIONS

Petrographical studies indicate that the copper sheets formed early during the burial history of the strata, prior to maximum compaction. The earliest alteration was to copper oxides indicating oxidizing porewater conditions. Subsequent sulphide and arsenide alteration products imply a more reducing environment as burial progressed. The association of the copper sheets with cross-fibre calcite veining suggests that they may have developed under overpressured porewater conditions which may have been generated during dewatering of the sediments during burial. Similarly, the copper oxide, arsenide and sulphide alteration products are also early, forming pre-compactional concretions as well as on the copper sheets. Reconstruction of the burial history of the Wessex Basin [12] indicates that these rocks would have achieved their maximum depth of burial by at least the end of the Lower Jurassic.

Therefore, the copper sheets and their alteration products are older than 176 Ma. The copper suffered alteration during the early burial history of the mudstones. However, the copper has been effectively isolated within the compacted clay matrix and unaffected by corrosion, retaining 30-80% of its original thickness, since that time -despite the probable presence of highly saline and reducing porewaters. Corrosion only recommenced when the rocks were uplifted and exposed to near surface weathering (probably only during the last few thousand years). These observations lend support to predictions of the long-term stability of copper in compacted bentonite.

ACKNOWLEDGEMENTS

This research was funded by the Swedish Nuclear Fuel and Waste Management Company (SKB) under SKB Contract No. 2248/1. AEM and MTS publish with the permission of the Director, British Geological Survey (NERC).

REFERENCES

1. L. Werme. *SKB Technical Report*, **TR 98-08**, Svensk Kärnbränslehantering AB (1998).
2. L.H. Johnson, J.C. Tait, D.W. Shoesmith, J. Crosthwaithe and M.N. Gray. *Atomic Energy of Canada Limited Report*, **AECL-10718** (1994).
3. F. King. *Applied Geochem.*,**10**, 477-487 (1995).
4. A. Bath, A. Milodowski, P. Ruotsalainen, E.-L. Tullborg, A Cortés Ruiz and J.-F. Aranyossy. *European Commission, Nuclear Science and Technology Report*, **EUR 19613 EN** (2000).
5. W. Miller, R. Alexander, N. Chapman, I McKinley and J. Smellie. *Natural Analogue Studies in the Geological Disposal of Radioactive Wastes*, Studies in Environmental Science 57, Elsevier, Amsterdam (1994).
6. Å. Bresle, J. Saers and B. Arrehnius. *SKBF/KBS Technical Report*, **TR 83-11**, Svensk Kärnbränslehantering AB (1983).
7. R. Hallberg, A.-G. Engvall and T. Wadsten. *British Corrosion J.*, **19**, 85-88 (1984).
8. R. Hallberg, P. Östlund and T Wadsten. *Applied. Geochem.*, **3**, 273-280 (1988).
9. N. Marcos. *Nuclear Waste Commission of Finnish Power Companies, Technical Report*, **YJT-89-18** (1989).
10. A.E. Milodowski, M.T. Styles and V.L. Hards. *SKB Technical Report*, **TR 00-11**, Svensk Kärnbränslehantering AB, 2000.
11. R.K. Harrison. *Bull. Geol. Survey Gr. Br.*, **52**, 1-26.
12. R.A. Chadwick, in *Atlas of Onshore Sedimentary Basins in England and Wales: Post-Carboniferous Tectonics and Stratigraphy*, edited by A Whittaker (Blackie & Sons Limited Publishers, Glasgow, 1985).

Simplified treatment of conditions for pitting corrosion of copper in chloride containing media.

Claes Taxén[1] and Ignasi Puigdomenech[2]
[1]Swedish Corrosion Institute, Kraeftriket 23 A, SE 10405 Stockholm, Sweden
[2]Department of Chemistry, Royal Institute of Technology, SE 10405 Stockholm, Sweden

ABSTRACT

Results from a simplified model of pitting corrosion of copper in chloride-containing waters are presented. The model is applicable for solutions with chloride concentrations between 0.02 M and 0.50 M. The criterion used for pitting is based on the solubility of $Cu_2O(s)$ in equilibrium with metallic copper and the diffusion of rates of the aqueous corrosion products. Compared with experimentally-determined potentials for breakdown of passivity, found in the literature, the calculated minimum potentials for propagation show good agreement for the pure chloride solutions. For mixed chloride/ hydrogen carbonate solutions the calculations indicate that pitting corrosion can propagate at potentials much lower than the potentials where breakdown of passivity has been observed.

INTRODUCTION

We have in preceding papers reported results from a model of pitting corrosion of copper [1]. The results are very complex and the values of the minimum potential required for propagation of pitting corrosion found, depend on a large number of variables. Among these variables are the concentrations of the major ions in the water considered. Combinations of the concentrations of chloride, sulphate, carbonate, sodium and calcium together with the bulk pH and oxygen content of the water, add up to a truly multi-dimensional result matrix. However, for a large group of waters, we find that the value of the minimum pitting potential is determined almost exclusively by the concentrations of chloride and carbonate and by the temperature. Having observed this as a result of previous calculations and studied the causes, we made a simplified model that is limited to chloride-rich waters. Although this simplified model does not give the same detailed information as the full model[1], the results in terms of the minimum potential required for propagation of pitting, are the same, within the limits for uncertainty. Furthermore, with this simplified treatment, we establish a transparent mathematical link between results and input values. It is not possible to give the minimum potential required for propagation of pitting as function of all the input data, as an explicit equation. The direct link to a limited set of equilibrium constants and diffusion coefficients is still very helpful when making sensitivity analyses.

THE MODEL

When pitting of copper is observed or when copper is corroding and not suffering pitting corrosion, the surface is generally covered by a layer of corrosion products. The innermost of these layers is composed of cuprous oxide, $Cu_2O(s)$. When pitting corrosion occurs, $Cu_2O(s)$ is frequently, but not always observed at the bottom of the pit. In order to determine limits for where copper is immune to pitting corrosion, we study the case where some cuprous oxide is

formed at the site of oxidation but at a fraction that may be insufficient to completely cover the underlying metal. If we for the present neglect the influence of cupric species, the following anodic processes may occur at the site of the oxidation:

$Cu(s) \rightarrow Cu^{+} + e^{-}$
$Cu(s) + \frac{1}{2} H_2O \rightarrow \frac{1}{2} Cu_2O(s) + H^{+} + e^{-}$
$Cu(s) + Cl^{-} \rightarrow CuCl(s) + e^{-}$

The products released into the solution (Cu^{+} and H^{+}) can directly react with components of the solution to give other aqueous species:

$Cu^{+} + n\ Cl^{-} \rightarrow CuCl_n^{1-n}$
$H^{+} + OH^{-} \rightarrow H_2O$
$H^{+} + CO_3^{2-} \rightarrow HCO_3^{-}$
$H^{+} + HCO_3^{-} \rightarrow H_2CO_3(aq)$

If we include all aqueous forms of cuprous species in Cu(I) and all protonated species, except water in H(I), we find that the fraction of the oxidised copper that is transported away from the site of the metal oxidation, by diffusion, can be expressed by equation (1).

$$tf = \frac{j_{Cu(I)}}{j_{H(I)} + j_{Cu(I)} - j_{Cl(-I)}} \qquad (1)$$

tf is the fraction of the corrosion products transported by diffusion and $j_{H(I)}$, $j_{Cu(I)}$, and $j_{Cl(-I)}$ denote the flux of protons, cuprous species and chloride, respectively, away from the site of oxidation. In the following we shall limit the study to cases where CuCl(s) does not form in the corrosion pit. It should be stressed that the omission of CuCl(s) may yield slightly more conservative estimates of the minimum potentials required for propagation of a corrosion pit. The complement to the transported fraction is the stationary fraction. A volume ratio between copper in the form of metallic copper and in the form of cuprous oxide shows that when the fraction of the oxidised copper that is stationary, that is, remains at the metal surface is higher than 0. 6 the metal surface is completely covered by the oxide. Consequently, when the fraction is lower than this value, there may be open pores in the oxide that allow a continuing process that may develop into a corrosion pit. During stationary conditions *tf* must be higher than 0.4 to maintain a local porosity of the $Cu_2O(s)$ layer. It is more convenient to treat the fluxes of aqueous corrosion products as ratios than as absolute values. The equation for *tf* is reformulated as:

$$tf = \frac{\frac{j_{Cu(I)}}{j_{H(I)}}}{1 + \frac{j_{Cu(I)}}{j_{H(I)}}} \qquad (2)$$

If we describe the ratio between the total flux of cuprous species and the total flux of protons in terms of the species in which they appear, we obtain:

$$\frac{jCu(I)}{jH(I)} = \frac{jCu^{+}}{jH^{+}} \cdot \frac{(1 + \frac{jCuCl(aq)}{jCu^{+}} + \frac{jCuCl_2^{-}}{jCu^{+}} + \frac{jCuCl_3^{2-}}{jCu^{+}} + \ldots)}{(1 - \frac{jOH^{-}}{jH^{+}} + \frac{jHCO_3^{-}}{jH^{+}} + 2 \cdot \frac{jH_2CO_3(aq)}{jH^{+}} + \ldots)} \qquad (3)$$

If we limit the study to cases where the free carbonate ion, CO_3^{2-}, and the sodium and calcium complexes with carbonate can be neglected, we find that the fluxes of hydrogen carbonate and

carbonic acid are equal in magnitude but opposite in sign. The hydrolysis of Cu^+ is not extensive but we can introduce the aqueous hydrolysis products too into the equation (3) and rearrange:

$$\frac{jCu(I)}{jH(I)} = \frac{jCu^+}{jH^+} \cdot \frac{(1 + \frac{jCuCl(aq)}{jCu^+} + \frac{jCuCl_2^-}{jCu^+} + \frac{jCuCl_3^{2-}}{jCu^+} + \frac{jCuOH(aq)}{jCu^+} + \frac{jCu(OH)_2^-}{jCu^+})}{(1 - \frac{jOH^-}{jH^+} + \frac{jH_2CO_3(aq)}{jH^+} - \frac{jCu^+}{jH^+}(\frac{jCuOH(aq)}{jCu^+} + 2 \cdot \frac{jCu(OH)_2^-}{jCu^+}))} \quad (4)$$

The flux density of an aqueous species can be written:

$$j = -\frac{CD}{RT}\frac{\partial \mu}{\partial x} \approx -D\frac{\partial C}{\partial x} \quad (5)$$

where C is the local concentration, D is the diffusion coefficient, R is the molar gas constant, T is absolute temperature and μ is the chemical potential. The approximation to Fick's first law is valid when the gradients in potential and in activity coefficients, are negligible. This is the case in the relatively concentrated solutions considered here and under the relatively mild conditions at the borderline case where a corrosion pit can just barely propagate. Using these equations to express the ratio between the flux of jCu^+ and jH^+:

$$\frac{jCu^+}{jH^+} = \frac{[Cu^+]D_{Cu^+}\frac{\partial \ln a(Cu^+)}{\partial x}}{[H^+]D_{H^+}\frac{\partial \ln a(H^+)}{\partial x}} \quad (6)$$

The ratio between the partial derivatives is, at equilibrium with $Cu_2O(s)$, determined by the solubility constant of $Cu_2O(s)$.

$$\frac{jCu^+}{jH^+} = \frac{D_{Cu^+}}{D_{H^+}} \cdot k_{1/2 Cu_2O}^{-1} \cdot \frac{\gamma_{H^+}}{\gamma_{Cu^+}} \quad (7)$$

The derivation of similar expression for all terms, appearing in equation (4), is a bit lengthy and we shall just give the results:

$$\frac{jCuCl_n^{1-n}}{jCu^+} = \frac{D_{CuCl_n^{1-n}}}{D_{Cu^+}} \cdot k_{CuCl_n^{1-n}} \cdot [Cl^-]^n \cdot \gamma_{Cl^-}^n \frac{\gamma_{Cu^+}}{\gamma_{CuCl_n^{1-n}}} \quad (8)$$

$$\frac{jCu(OH)_n^{1-n}}{jCu^+} = \frac{D_{Cu(OH)_n^{1-n}}}{D_{Cu^+}} \cdot k_{Cu(OH)_n^{1-n}} \cdot a_{H^+}^{-n} \frac{\gamma_{Cu^+}}{\gamma_{Cu(OH)_n^{1-n}}}(1-n) \quad (9)$$

$$\frac{jOH^-}{jH^+} = -\frac{D_{OH^-}}{D_{H^+}} \cdot \frac{\gamma_{H^+} \cdot k_w}{\gamma_{OH^-} \cdot a_{H^+}^2} \quad (10)$$

$$\frac{jH_2CO_3}{jH^+} = \frac{D_{HCO_3^-}}{\frac{D_{H^+}}{\gamma_{H^+}}} \cdot \frac{[CO_2]_{tot}(1 - \frac{(1 - \frac{D_{HCO_3^-}}{D_{H_2CO_3}})}{(1 + \frac{k_{H_2CO_3}}{k_{HCO_3^-}} \cdot a_{H^+_{bulk}} \cdot \gamma_{HCO_3^-})}) \cdot \frac{k_{H_2CO_3}}{k_{HCO_3^-}} \cdot \gamma_{HCO_3^-}}{(\frac{k_{H_2CO_3}}{k_{HCO_3^-}} \cdot a_{H^+} \cdot \gamma_{HCO_3^-} + \frac{D_{HCO_3^-}}{D_{H_2CO_3}})^2} \quad (11)$$

Equilibrium constants and diffusion coefficients

Table I shows the equilibrium constants and the diffusion coefficients used in the present study. The equilibrium constants are calculated from a recent compilation of thermodynamic data for copper compounds and aqueous complexes [2]. Since diffusion coefficients always appear in pairs, as a ratio, in equations 7 to 11, it is sufficient to use the values of the diffusion coefficients at 25 °C. Although the actual value of the diffusion coefficient increases with temperature, a ratio between diffusion coefficient is to a first approximation, independent of temperature.

Activity Coefficients

The activity coefficients, γ, were calculated from the ionic strength, *I*, using Davies' method [3]:

$$\lg \gamma_i = A \cdot z_i^2 \left(\frac{\sqrt{I}}{1 + \sqrt{I}} - 0.2 \cdot I \right) \qquad (12)$$

A is a constant with the value 0.51 at 25°C and 0.56 at 75°C, *z* is the charge of the species.

Table I. The equilibrium constants [2] and the diffusion coefficients used in the present study.

$D*10^5$ (cm^2/s)	lg *k*								
	25°C	5°C	25°C	50°C	75°C	H^+	Cl^-	CO_3^{2-}	Cu^{2+}	$H_2(g)/2$
H^+	9.31					1				
CO_3^{2-}	0.92							1		
OH^-	5.27	-14.73	-14.00	-13.28	-12.72	-1				
HCO_3^-	1.18	10.55	10.33	10.17	10.11	1		1		
CO_2(aq)	1.92	17.06	16.68	16.46	16.44	2		1		
Cu^+	0.54	2.77	2.83	2.92	3.02	-1			1	1
CuOH(aq)	0.54	-10.10	-8.72	-7.34	-6.26	-2			1	1
$Cu(OH)_2^-$	0.54	-13.34	-13.35	-13.23	-13.00	-3			1	1
CuCl(aq)	0.54	6.01	6.14	6.25	6.33	-1	1		1	1
$CuCl_2$-	0.54	8.63	8.45	8.33	8.29	-1	2		1	1
$CuCl_3^{2-}$	0.54	8.01	7.69	7.50	7.47	-1	3		1	1
Cu(s)		12.22	11.40	10.52	9.77	-2			1	2
Cu_2O(s)		7.34	7.16	6.96	6.79	-4			2	2
CuCl(s)		9.90	9.43	8.99	8.66	-1	1		1	1
e^-		0	0	0	0	-1				1

Results

Together with data from table I, equations 2 and 4 to 12 allow the factor *tf*, as a function of the pH in the pit, to be calculated from properties of the bulk solution. Figure 1 shows the calculated values of *tf*, as function of pit pH, for two different compositions of the bulk solution. The diagram shows that *tf* increases monotonously with decreasing pit pH. For the higher chloride concentration, 0.1 M, about pH 5.1 must be reached to attain the limiting value for pit propagation (*tf*=0.4) whereas pH 4.8 must be reached for the lower chloride concentration. A basic assumption in this paper is that cuprous oxide is stable at the bottom of the pit. Cu_2O(s) is formed under pitting conditions but in amounts that are insufficient to completely cover the underlying metal. The minimum potential required for the formation of Cu_2O(s) is given by the

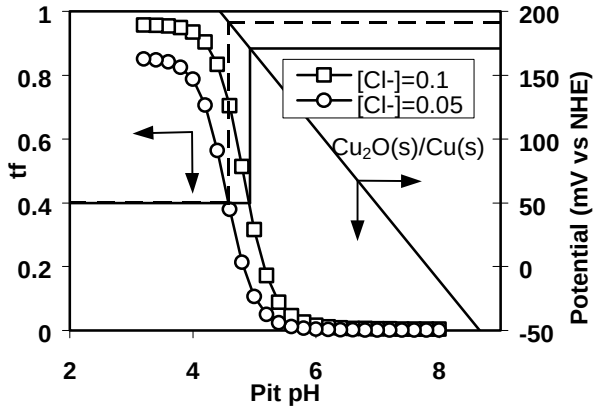

Figure 1. Calculated values of *tf* as function of the local pH. 25 °C and $[CO_2]_{tot}$ =0.064 M in the bulk.

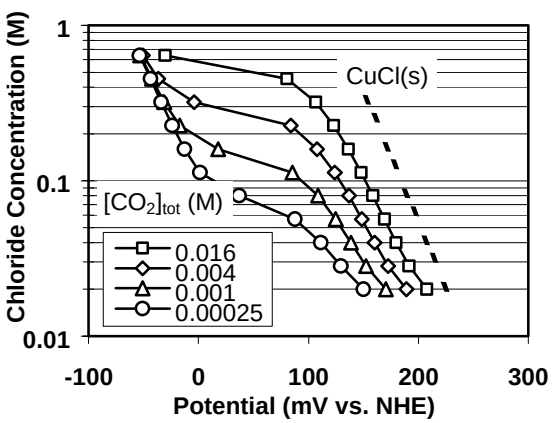

Figure 2. Minimum pitting potentials as function of the chloride concentration in the bulk, 25 °C, total carbonate concentration in the bulk varied

equilibrium line $Cu_2O(s)/Cu(s)$. The intersection with this line at pH 4.8 and pH 5.1 give 160 mV and 182 mV respectively. These are the minimum pitting potentials for the two water compositions considered. Figure 2 shows the minimum pitting potentials as function of chloride concentration for various total carbonate concentrations.

Comparison of results to published electrochemical data

Figure 3 shows the minimum pitting potential calculated by the simplified model for a chloride solution without carbonate. Experimentally determined potentials for breakdown of passivity from the literature [4] are also shown in the diagram. Figures 4 and 5 show the temperature dependence of the minimum pitting potential for solutions where the total carbonate concentration is equal to the chloride concentration. Corresponding values of experimentally determined potentials for breakdown of passivity from the literature [5,6] are also shown in the diagrams.

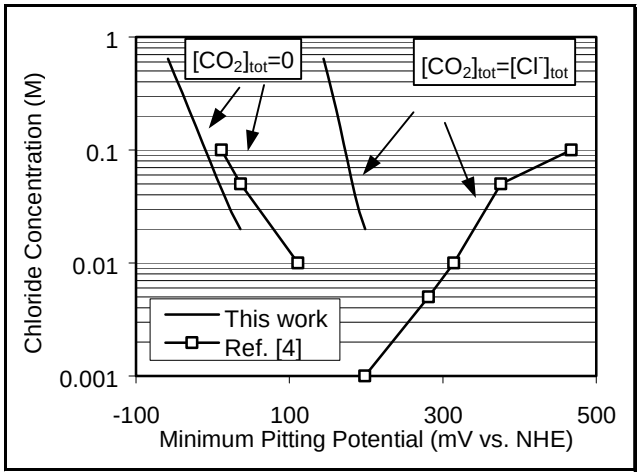

Figure 3. Minimum pitting potential as function of the chloride concentration. Values calculated by the simplified model for a water without carbonate and experimentally determined potentials for breakdown of passivity from the literature [4], 25 °C.

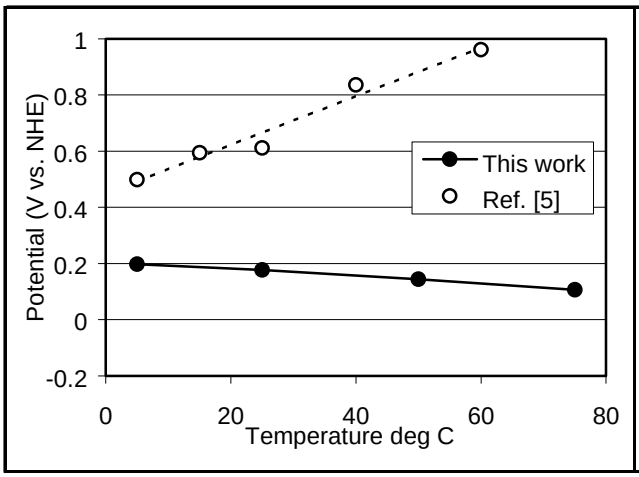

Figure 4. Minimum pitting potential as function of the temperature. Values calculated by the simplified model for a solution with 0.1 M chloride and 0.1 M total carbonate and experimentally determined potentials for breakdown of passivity from the literature [5].

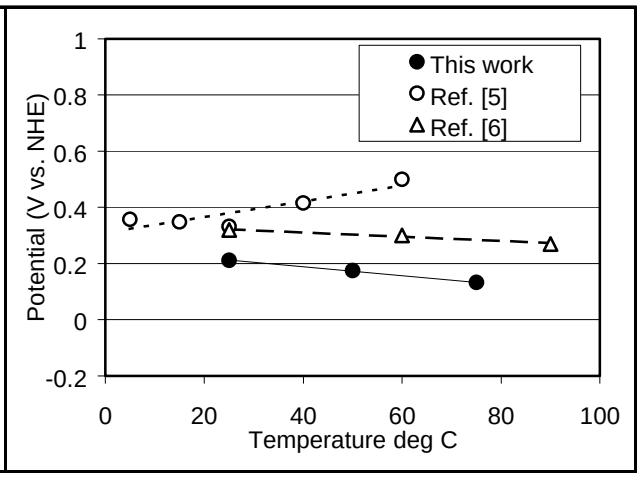

Figure 5. Minimum pitting potential as function of the temperature. Values calculated by the 'full model' for a solution containing 0.01 M chloride and 0.01 M total carbonate and experimentally determined potentials for breakdown of passivity from the literature [5,6].

CONCLUSIONS

In pure chloride solutions, the calculated values of the minimum potential for propagation of pitting agree well with experimentally determined values for the potential of breakdown of passivity, found in the literature. The addition of carbonate to the solutions increases the value of the minimum potential for propagation. The potential of breakdown of passivity has a stronger dependence on the carbonate concentration.

ACKNOWLEDGEMENT

This work was supported by the Swedish Nuclear Fuel and Waste Management Co. (SKB).

REFERENCES

1. a.) C. Taxén Pitting Corrosion Of Copper . Equilibrium - Mass Transport Limitations. Scientific Basis for Nuclear Waste Managment XXIII : Symposium Held November 29-December 2, 1999, Boston, Massachusetts, U.S.A. (Materials Research Society). Eds. Robert W. Smith, David W. Shoesmith, b.) KI-rapport 1996:8E. Swedish Corrosion Institute, c.) 13:th International Corrosion Conference, Nov 25-29, 1996, Melbourne Australia. Proceedings, Paper 141.
2. I. Puigdomenech and C. Taxén, Thermodynamic data for Copper, Implications for the corrosion of copper under repository Conditions. SKB Technical Report TR-00-13, Swedish Fuel and Waste Management Co. 2000.
3. W. Stumm and J.J. Morgan, in *Aquatic Chemistry* 2.nd ed. (Wiley, New York, 1981) p. 135.
4. M. Drogowska, L. Brossard and H. Menard. *J. Electrochem Soc.* **139** pp. 39-47 (1992)
5. M. Drogowska, L. Brossard and H. Menard. *J. Electrochem Soc.* **140** pp. 1247-1251 (1993)
6. J. G. N. Thomas and A. K. Tiller, *Br. Corros. J.* **7**, 256 (1972).

The Resistance of Pure Copper to Stress Corrosion Cracking in Repository Environments

Bo Rosborg[1] and Lars Werme
Svensk Kärnbränslehantering AB, P.O. Box 5864,
SE-102 40 Stockholm, Sweden
[1]Rosborg Consulting, Östra Villavägen 3,
SE-611 36 Nyköping, Sweden

ABSTRACT

The risk for stress corrosion cracking (SCC) of the copper canister in the final repository for high-level radioactive waste in Sweden is low. However, it is a desire to try to elucidate and if possible quantify this minor risk.

Available information from others and own work is discussed together with possible methods to estimate the resistance of pure copper to SCC in repository environments. An attempt to rationalise available crack growth rate data is made.

Electrochemically controlled slow strain rate testing of pure copper was performed in a sodium nitrite solution, known to give SCC, and in a synthetic groundwater of pH 9. For reasons of comparison, testing was also performed in air. Whereas the occurrence of SCC as expected was clear in the sodium nitrite solution, it cannot be claimed that SCC has occurred in the synthetic groundwater.

INTRODUCTION

A KBS-3 repository [1]

The strategy is to enclose the spent fuel in tightly sealed canisters that are embedded in clay about 500 m down in the Swedish bedrock, see figure 1a. The rock provides a stable and durable environment where changes occur very slowly. The canister isolates the fuel from the groundwater. The clay prevents groundwater flow around the canister while protecting against minor movements in the rock.

The copper canister [2]

The copper canister, see figure 1b, consists of a five centimeter thick copper casing with a cast iron insert to provide mechanical strength. It is manufactured from plate of pure oxygen-free copper with a deliberate addition of a small amount of phosphorus to improve creep properties. The dimensions and waste load of each canister have been chosen such that the temperature on the outer surface of the canister never exceeds 100ºC.

Stress corrosion cracking

It has been shown that stress corrosion cracking (SCC) can occur in copper (of commercial quality) [3-4]. Nitrite and ammonia are examples of species harmful to copper [3]. It is not a very sensational circumstance that copper can be sensitive to SCC considering today's knowledge, and does not in any way disqualify it as a material for the canister. Most materials, if not all, show susceptibility under some circumstances. The objective is to assure that these circumstances do not appear in the intended application.

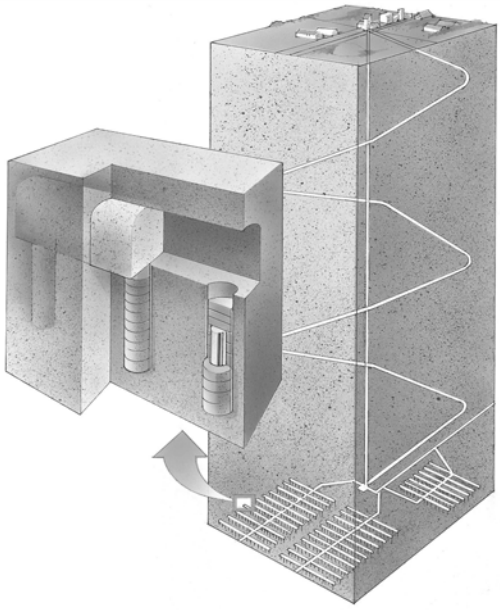

Figure 1a. A KBS-3 repository.

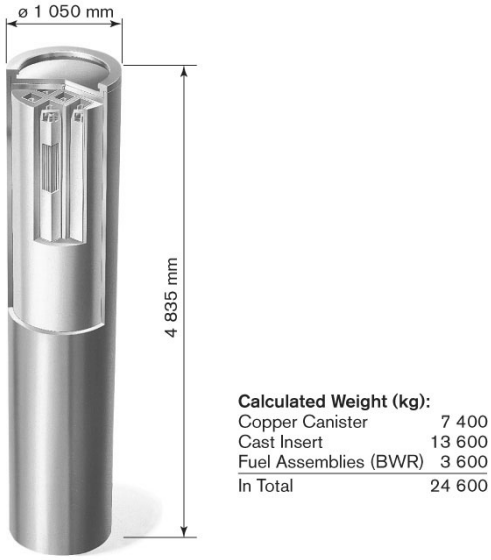

Figure 1b. The copper canister.

The near-field environment

The chemical environment in the immediate vicinity of the canister is determined by the composition of the bentonite pore water and its interaction with the groundwater in the surrounding rock. The deep granitic groundwaters in Sweden are oxygen-free. During the construction of the repository and some limited period after that, there will be oxygen present in the repository. The time required to consume the oxygen in the bentonite has been calculated to be in the range 10 to 300 years [5].

Life prediction

No known corrosion processes should be able to violate the integrity of the canister for at least 100 000 years.

It is of course exceedingly difficult to predict life of the order of hundreds of thousands years, in particular concerning such a life-limiting phenomenon as SCC. The consumption of material is none or minor during the attack, which does not allow material balances to be used to predict life as for general corrosion. Nor give crack growth rate measurements straight off a practicable way of approach. The lowest crack growth rates that can be measured with the best available technique (say 10^{-12} m/s) correspond to a crack growth of several decimeters in hundred thousand years [6-7]. Thus, one is referred to indirect methods and extrapolations.

CRACK GROWTH RATE DATA

The strict requirements

Standardized and recommended procedures to produce valid crack growth rate data exist (see for instance ISO 7539-6). These consider specimen dimensions (as to requirement on plane strain), evaluation of crack extension, out-of-plane cracking, extent of crack branching, and others. The historical background is requirements to produce valid fracture toughness data. The need to follow the strict requirements in all details for environmentally assisted cracking is still an open question.

Available data

Three sources of crack growth rate data for pure copper in different environments are found in the literature [7-13]. Disregarding the strict requirements above all available crack growth rate data are considered in the following attempt to rationalise the data. Figure 2a shows a template reflecting different lifetime requirements. In figures 2b through 2d the available data are shown for the different methods of loading.

Threshold stress intensity factors

Any crack growth was not found for self-loaded specimens after 142 to 265 days of exposure in either a nitrite or an ammonia containing environment at a stress intensity of 22 $MPa \cdot m^{½}$ [9], see figure 2b. Thresholds of about 16, 24-27 and 30 $MPa \cdot m^{½}$ are shown from constant load testing of cold-worked material in sodium nitrite solutions [7-13], see figure 2c. (The specimen thickness was 7.6, 15 and 25 mm respectively, and the solutions and test procedures differ.) For constant extension rate testing in nitrite solutions crack growth has been reported at a stress intensity as low as 10 $MPa \cdot m^{½}$ [9]. For experimental details see refs. 7-13.

RESULTS FROM SLOW STRAIN RATE TESTING (SSRT)

Experimental details

Electrochemically controlled SSRT of pure copper was performed in a 0.3 M $NaNO_2$ solution, known to give SCC [14], and in a bentonite equilibrated synthetic groundwater of pH 9, see table I. For reasons of comparison, testing was also performed in air. All chemicals used to prepare the solutions were of pro analysi quality.

Plain cylindrical uniaxial tensile specimens of two pure copper alloys were tested, named Cu-OF (UNS 10100; EN133/63:1994 Cu-OF1) and Cu-OFP (unofficial SKB designation). The latter alloy is UNS 10100 copper with a deliberate addition of 40 ppb P. The materials were received in the form of pieces from thick plates and have been tested in the as-received condition. The specimen gauge section (Ø4 x 25 mm) was carefully turned and no further working operation was performed. The specimens were ultrasonically cleaned in acetone and alcohol.

After a preexposure in the solution for one day, the specimen was polarized to the preselected potential by means of a potentiostat and the SSRT was started. A saturated calomel electrode (SCE) was used as the reference electrode, and a platinum ring as the counter electrode. A nominal strain rate of $4 \cdot 10^{-7}$ s^{-1} was used. With a few exceptions the specimens were pulled to failure in the solution. For further experimental details see ref. 15.

Results

The results from the SSRT of the Cu-OF alloy in the 0.3 M $NaNO_2$ solution are shown in figure 3a. A strong potential dependence is evident; while SCC was observed at E_{corr} in deaerated solution, no SCC was observed at –150 mV SCE. The fractographs in figures 4a and b reveal both intergranular and transgranular cracking.

The results from the SSRT of both alloys in the synthetic groundwater are shown in figure 3b. A very low tendency to SCC, if any (compared to the nitrite solution), was observed. No susceptibility to SCC was revealed at E_{corr} in deaerated solution. An influence of the environment on the degree of surface attack was, however, observed at higher potentials, compare fractographs in figures 4d through f.

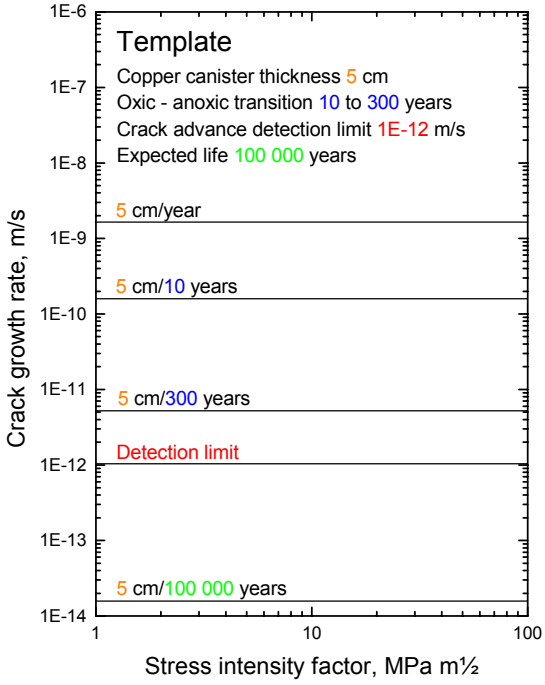

Figure 2a. Template for available crack growth rate data.

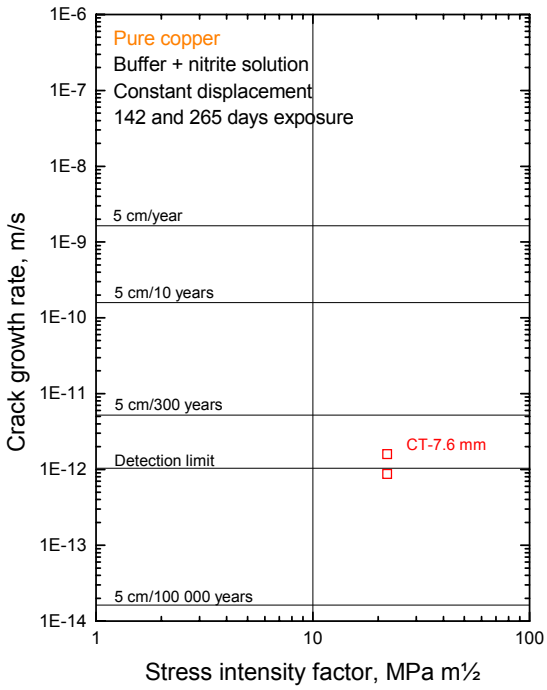

Figure 2b. Constant displacement.

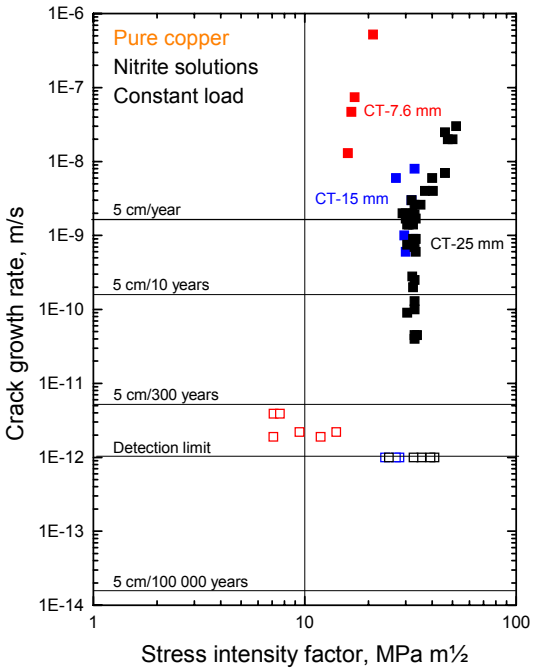

Figure 2c. Constant load.

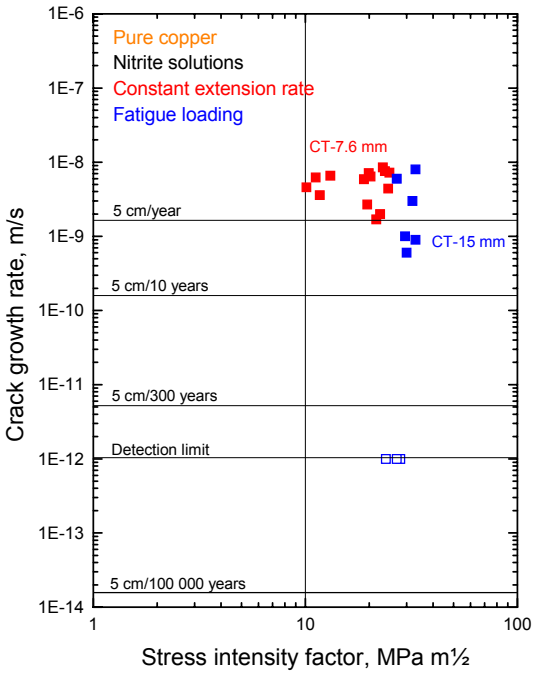

Figure 2d. Straining.

Table I. Composition of the bentonite equilibrated synthetic groundwater (in mM/ppm).

Na^+	Ca^{2+}	NH_4^+	Cl^-	HCO_3^-	SO_4^-	pH
750/17 240	0/0	0.03/0.5	540/19 200	10/600	100/9600	9.03

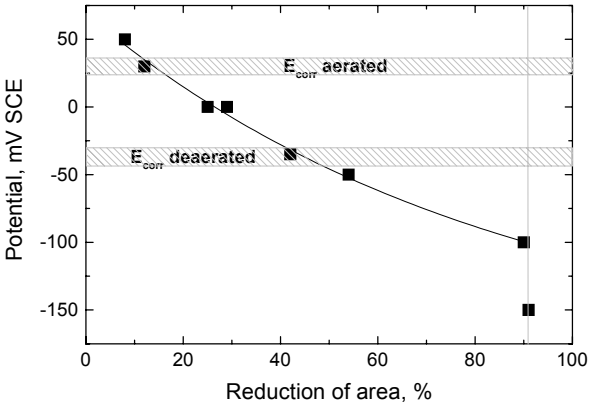

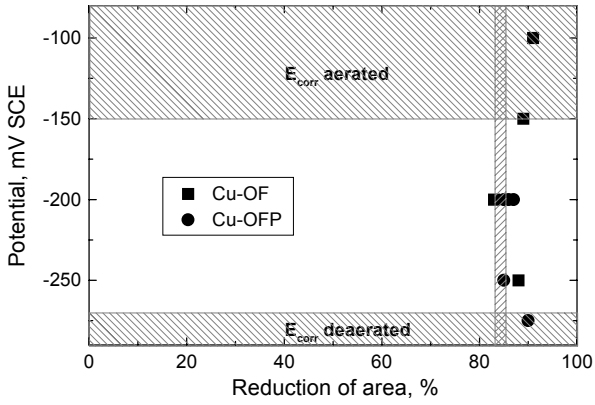

Figure 3a. Results from SSRT of the Cu-OF material in 0.3 M $NaNO_2$ solution at room temperature and a nominal strain rate of $4 \cdot 10^{-7}$ s^{-1}. (The vertical line marks the reduction of area for a single specimen tested in air at a nominal strain rate of $5 \cdot 10^{-6}$ s^{-1}.)

Figure 3b. Results from SSRT of the Cu-OF and the Cu-OFP materials in the synthetic groundwater and in air at room temperature and a nominal strain rate of $4 \cdot 10^{-7}$ s^{-1}. (The vertical band marks the reduction of area for four specimens of the Cu-OFP material tested in air at room temperature.)

DISCUSSION

Material selection

The copper grade of interest is pure oxygen-free copper containing 40-60 ppm P. Phosphorus has been reported to be harmful for stress corrosion resistance, however, the deliberate addition is believed to be well below any harmful amount [16].

Present crack growth rate data

High SCC growth rates have been reported. So is the case for reactor pressure vessel steels in high temperature water, without being a cumbersome problem in practice [6]. An observation of susceptibility to SCC in laboratory testing does not necessarily mean problems in practice. Care should be taken, however, to avoid in the intended application the circumstances that promote SCC.

Extensive databases with crack growth rate data for other material – environment systems often show a wide apparent scatter [6]; it is, therefore, not unexpected that the present crack growth rate data, even though few, show a certain scatter. Experimental variations, often environmental, make the difference.

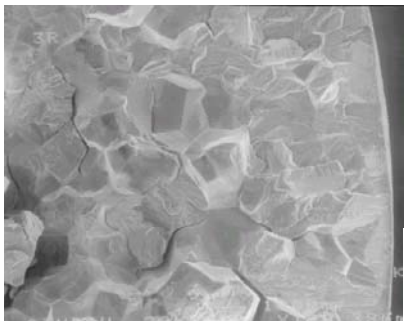

a. E_{corr} in aerated nitrite solution

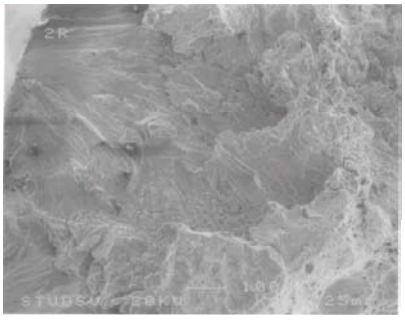

b. E_{corr} in deaerated nitrite solution

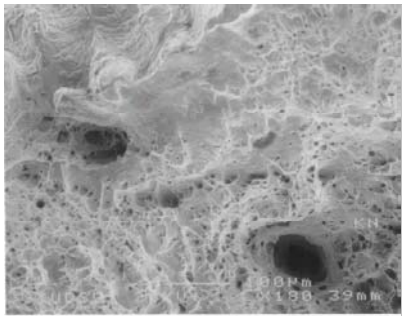

c. -150 mV SCE in nitrite solution

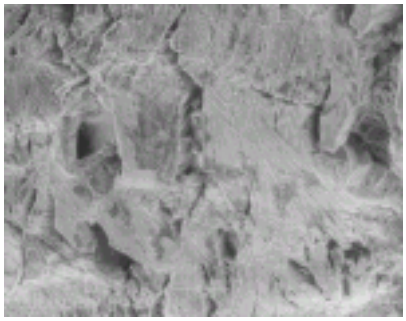

d. -200 mV SCE

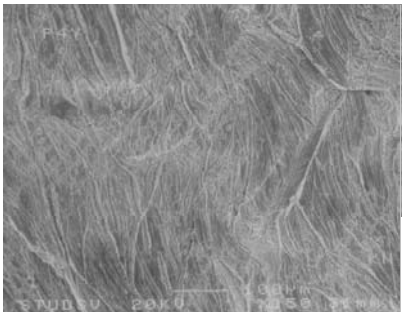

e. E_{corr} in deaerated solution

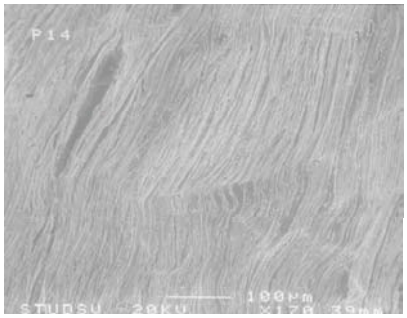

f. Air

Figure 4a-f. Fractographs from specimens tested in 0.3 M $NaNO_2$ solution (see figure 3a), and micrographs from surfaces of specimens tested in synthetic groundwater (see figure 3b) and in air at RT and a nominal strain rate of $4 \cdot 10^{-7}$ s^{-1}.

Possible methods for life prediction

Since copper is thermodynamically stable in pure water, the extent of corrosion will be controlled by the supply of corrodents from the environment. Possible methods for life prediction are:

- use the fracture mechanics approach – cracks may exist after manufacture or form later, but the growth should be sufficiently slow; requirements: non-destructive testing records/crack growth rate data/thresholds/extrapolations
- make initiation or crack growth impossible – avoid harmful species (and secure beneficial species); requirements: in depth knowledge of the factors that influence the susceptibility to cracking
- limit crack growth – establish mass transport limitations; requirements: in depth knowledge of the factors that influence the susceptibility to cracking, limit loading conditions

CONCLUSIONS

High crack growth rates can be obtained in pure copper for certain environmental and loading conditions, such as the presence of nitrite. Available data shows, unfortunately, no agreement for stress intensity factor thresholds.

The occurrence of SCC was, as expected, clear after accelerated stress corrosion testing of pure copper (by means of SSRT) in a sodium nitrite solution. It cannot be claimed, however, that SCC has occurred during the comparative testing of pure copper in a bentonite equilibrated synthetic groundwater with the very same experimental conditions, but for the environment.

The present results do not call in question the intention to manufacture the canister of pure copper. However, since SCC is such a treacherous phenomenon, every precaution should be taken to assure that harmful circumstances do not appear in the final repository.

ACKNOWLEDGMENTS

The assistance of Miss Julia Grigorieva and Mrs Britt-Marie Svensson at Studsvik Material AB in performing the slow strain rate testing is gratefully acknowledged.

REFERENCES

1. SR 97 Waste, repository design and sites, Swedish Nuclear Fuel and Waste Management Co, Technical Report TR-99-08, 1999.
2. L. Werme, Design premises for canister for spent nuclear fuel, Swedish Nuclear Fuel and Waste Management Co, Technical Report TR-98-08, 1998.
3. F. King, The potential for stress corrosion cracking of copper containers in a Canadian nuclear fuel waste disposal vault, Atomic Energy of Canada Limited, 1996 (AECL-11550, COG-96-94).
4. J. C. Farmer, R. A. Konynenburg, R. D. McCright and G. E. Gdowski, Survey of degradation modes of candidate materials for high-level radioactive-waste disposal containers. Volume 4. Stress corrosion cracking of copper-based alloys, Lawrence Livermore National Laboratory, California, 1988 (UCID-21362 Vol 4).
5. P. Wersin, K. Spahiu and J. Bruno, Time evolution of dissolved oxygen and redox conditions in a HLW repository, Swedish Nuclear Fuel and Waste Management Co, Technical Report TR-94-02, 1994.
6. B. Rosborg, Possibilities and limitations with the modern techniques to measure crack growth rates, Proc Inter Symp on Plant Aging and Life Prediction of Corrodible Structures, May 15-18, 1995, Sapporo, Japan, pp. 365-370.
7. K. Pettersson and M. Oskarsson, Stress corrosion crack growth in copper for waste canister applications, Mat. Res. Soc. Symp. Proc. **608**, 95 (2000).
8. K. Pettersson and M. Oskarsson, A study of stress corrosion crack growth in copper for nuclear waste canister application, Royal Institute of Technology, Stockholm 1997 (TRITA-MAC-0611), SKB, Stockholm 1997 (97-3420-25).
9. F. King, C. D. Litke and B. M. Ikeda, The effects of oxidant supply and chloride ions on the stress corrosion cracking of copper, Ontario Power Generation, Toronto 1999 (Report No: 06819-REP-01200-10013-R00).
10. F. King, C. D. Litke and B. M. Ikeda, The stress corrosion cracking of copper nuclear waste containers, Mat. Res. Soc. Symp. Proc. **556**, 887 (1999).
11. F. King, C. D. Litke and B. M. Ikeda, The stress corrosion cracking of copper containers for the disposal of high-level nuclear waste, CORROSION/99, NACE International, Houston, TX, paper no 482, 1999.

12. S. Hietanen, U. Ehrnstén and T. Saario, Environmentally assisted cracking behaviour of copper in simulated ground water, Finnish Centre for Radiation and Nuclear Safety, Helsinki May 1996 (STUK-YTO-TR 105).
13. S. Hietanen, Environmentally assisted cracking behavior of copper in simulated ground water. VTT Manufacturing Technology, Espoo 1993 (VTT-MET B-232, in Finnish).
14. L. A. Benjamin, D. Hardie and R. N. Parkins, Br Corros J **23**, 89 (1988).
15. B. Rosborg, The resistance of the copper canister to stress corrosion cracking, Studsvik Material AB, STUDSVIK/M-98/100, December, 1998.
16. D. H. Thompson and A. W. Tracy, J Metals (Trans) **1**, 100 (1949).

Sulfide Corrosion of Copper Canister for Spent Fuel Disposal

I. Escobar, C. Silva, E. Silva and L Werme[1]
Comisión Chilena de Energía Nuclear (CCHEN), Amunátegui N° 95, Santiago, Chile.
[1]Svensk Kärnbränslehantering AB (SKB), Box 5864, SE-10240 Stockholm, Sweden.

ABSTRACT

Svensk Kärnbränslehantering (SKB) has chosen copper as the corrosion barrier material in the waste package for disposal of spent nuclear fuel in Sweden. The reason for this choice is that copper is immune to corrosion in oxygen free water over a relatively wide composition range. Some species in the groundwater may upset this stability and dissolved sulfides are one of the most important ones in deep granitic groundwaters in Sweden. In the present paper we present XPS analysis of copper, which has been polarized at different potentials in 1 ppm and 100 ppm sulfide solutions. Only at the highest sulfide concentrations (100 ppm) could we clearly observe adherent sulfides as corrosion products. The failure to do so for lower sulfide concentrations was probably caused by too high levels of residual oxygen. For future studies of the formation and the stability of sulfide corrosion products formed through corrosion in sulfide containing groundwaters with sulfide concentrations in the expected range it will be important to ensure that the water is oxygen free and reducing.

INTRODUCTION

In Sweden, SKB plans to encapsulate spent nuclear fuel in canisters that have an inner cast iron component for mechanical strength and an outer copper shell for corrosion protection [1]. Posiva in Finland will use a similar canister for the Finnish spent nuclear fuel [2]. This canister will be buried, surrounded by compacted bentonite clay, in tunnels in granitic rock [3].

During the construction of the repository and some limited period after that, there will be oxygen present in the repository. The oxygen will be consumed through reactions with minerals in the bentonite and in the host rock, but bacterial activity will be most effective in consuming oxygen in the surrounding rock [4] and most likely also in the tunnels and shafts. In the compacted bentonite closest to the canisters, however, survival of bacteria is unlikely [5,6].

Copper is thermodynamically stable in oxygen-free water and once the oxygen is gone, copper is immune to corrosion. This immunity can be upset if the water contains dissolved sulfide or very high concentrations of chloride in combination with low pH. High chloride concentrations (> 1 mol/dm^3) can be found in deep granitic groundwaters in Scandinavia and the consequences of this need to be studied further. The major concern, however, for the long term corrosion resistance of the spent fuel canister is the groundwater's sulfide content, which can be up to 0.2 mmol/dm^3. SKB has recently published a review of the thermodynamic data for copper [7]. Figure 1 shows a Pourbaix diagram for copper in solutions containing dissolved sulfide. The diagram shows that in the pH range (6.5 – 10) and E_H range (-200 mV - -300 mV) expected in the repository, copper sulfides are stable. The canister corrosion will most likely be controlled by the availability of sulfide at the canister surface and not by the rate of reaction of sulfide with copper. Understanding the kinetics and mechanisms controlling the sulfidation of copper are, nevertheless, of importance for assessing the long-term corrosion a spent fuel canister in the repository. The majority of the studies of the behavior of copper and copper alloys in sulfide containing water have dealt with sulfide polluted seawater. These studies are in most cases not

applicable to the corrosion on copper canisters since they concern alternating oxidizing and reducing conditions. Some electrochemical studies of early stages of film formation on copper in sulfide environments have been published [8,9]. There are also studies performed freely corroding conditions offering various explanations for the processes determining the corrosion potential [8, 10, 11, 12]. These studies are not directly focussed on nuclear waste management. Several studies have, therefore, been initiated both by the regulatory agencies in Sweden and Finland [13, 14] as well as by others [15, 16].

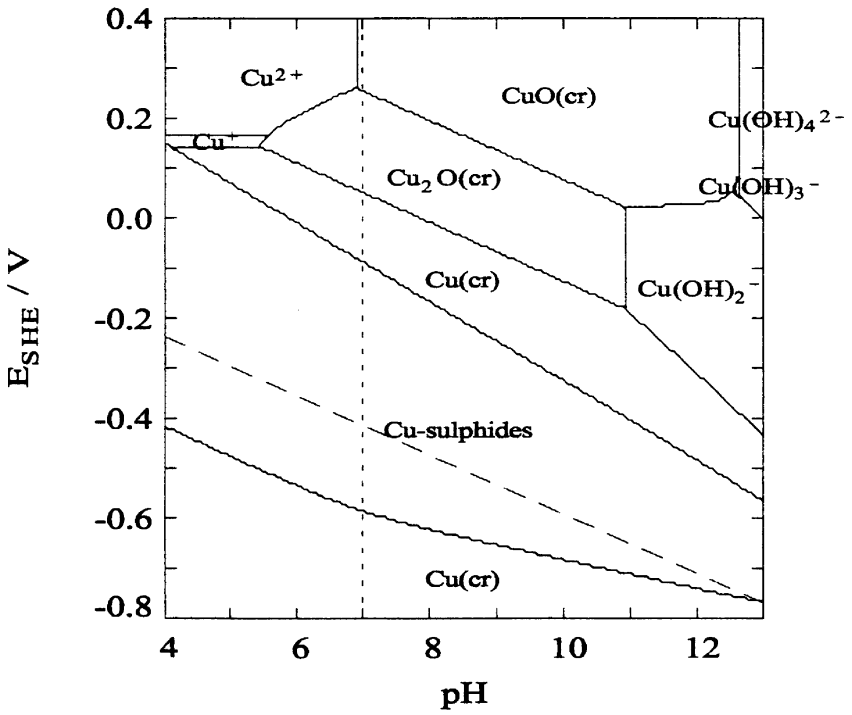

Figure 1. Pourbaix diagram for copper in solutions containing $[HS^-]_{TOT}$ = 0.2 mmol/kg and $[Cu]_{TOT} = 10^{-6}$ mol/kg at 25°C (from ref. 7).

Escobar et al. [16] used cyclic voltammetry and Tafel slope measurements to study copper corrosion in waters containing sulfide. They used two electrolytes, which simulated the expected bentonite pore water composition, one with a typical sulfide concentration (10^{-5} mol/dm^3) and one with an enhanced sulfide concentration (1mmol/dm^3). They also used two pure sulfide solutions, both with concentrations higher or much higher that found in natural waters (1mmol/dm^3 and 100 mmol/dm^3). From the Tafel curves, Escobar et al. determined the corrosion potential and the corrosion rates for the sulfide concentrations 1mmol/dm^3 and 100 mmol/dm^3 in the temperature range 15 to 90°C. The corrosion potentials at 25°C were found to be –1.08 V_{SCE} for 100 mmol/dm^3 sulfide and –0.96 V_{SCE} for 1mmol/dm^3 sulfide. These corrosion potentials compare quite well with those measured by King and Stroes-Gascoyne, who measured a corrosion potential of –0.90 V_{SCE} in a 0.3 mmol/dm^3 (10 ppm) HS^- solution and –0.96 V_{SCE} in a 3.3 mmol/dm^3 (100 ppm) HS^- solution.

The corrosion rates calculated by Escobar et al. were very high, ranging from almost 10 to 100 μm per year; the highest rates were obtained for 100 mmol/dm^3 and 90^{o}C. These represent maximum corrosion rates if there are no transport limitations for the transfer of sulfide to the copper surface. Such a situation could occur if a biofilm of sulfate reducing bacteria formed on the canister surface.

Hilden et al. [13] performed cyclic voltammetric measurements and surface characterization of copper exposed to water with 10 ppm H_2S at pH 8.9 (0.1 mol/dm^3 borax as buffer) at 80^{o}C and 2 MPa pressure. The surface film thickness was calculated from the charge consumed in reduction. This showed that the average thickness of the surface film formed in the presence of 10 ppm H_2S was roughly 10 times thicker than the film formed in a pure borax solution. Hilden et al. also studied the surface film stability by monitoring the resistance and open circuit potential of a previously formed film. Their conclusions were that the experimental data indicated that 10 ppm of H_2S in 0.1 mol/dm^3 borax was not enough to promote the formation of three-dimensional copper sulfide films. The small indications of surface reactions and layers in the potential area where copper sulfides should form are likely to be caused by adsorption of sulfide on the surface, and not by the formation of a three dimensional sulfide film. They also found that 10 ppm H_2S in the solution resulted in the formation of a much more defective film than in a pure borax solution.

Hermansson & Eriksson [14] describe a long-term experiment (> 6 months), where copper is exposed to synthetic groundwaters in a closed system. Two of those waters, with chloride concentrations of about 80 ppm and about 8000 ppm respectively, contained sulfide additions in the form of Na_2S to a concentration of 41 ppm (as S^{2-}). The temperature in the experiments was 20^{o}C and the starting pH 8.5. In the subsequent analysis of the corrosion products Hermansson and Eriksson observed that the corrosion products contained very little sulfur and that copper and oxygen were the dominating elements. They also conclude that the surface film formation is much faster in the presence of sulfide than in the absence of sulfide, minutes to hours compared to weeks and months.

PRESENT EXPERIMENTAL WORK

In the present paper we present XPS analysis of copper, which has been polarized at different potentials in 1 ppm (0.03 mmol/dm^3) and 100 ppm (3.3 mmol/dm^3) sulfide solutions. Figures 2 shows an XPS spectrum of the binding energy range 0 to 550 eV of a copper sample that has been polarized at –0.9 V_{SCE} for 30 minutes after 5 min. Ar ion sputtering to remove the outermost surface layer. The copper coupons had to be transported from CCHEN's own electrochemistry laboratories to a University Laboratory for XPS analysis and they likely picked up a thin surface contamination from the atmosphere during that time. This can be seen in the quite intense oxygen and carbon 1s signals. The carbon 1s peak, which is often referred to as spurious or adventitious carbon, is reliably found at a binding energy of 284.8 eV. It is caused by hydrocarbon contamination and is unavoidable on any sample that exposed to normal atmosphere. During the 1970s, it was frequently used as an internal standard for energy calibration. We also used the C 1s peak for our energy calibration. Signals from sulfur are visible, although quite weak. After Ar sputtering, however, the intensity of the carbon peak is reduced considerably. The oxygen signal is also reduced to some extent and the sulfur 2s and 2p peaks are quite prominent. The binding energies of the S 2s and 2p correspond to sulfide sulfur.

Copper polarized at –0.75 V (SCE) for 30 minutes also had indications of sulfide on the surface, although weaker that what was found for –0.9 V. For copper surfaces exposed to solutions with only 1 ppm sulfide, no sulfide was detected. Only oxygen signals could be found.

The experiments were performed without strict measures to exclude oxygen. It is, therefore, possible that both both oxides and sulfides could form on the surfaces. The copper binding energies in sulfides and oxides are very close and it was impossible to determine whether either or both Cu(I) oxides and sulfides were present on the copper surfaces of any of the samples. On one sample exposed to 1 ppm sulfide solution and polarized at -0.5 V (SCE) for 30 minutes the typical Cu 2p peaks of a Cu(II) oxide were detected. This is shown in Figure 3.

DISCUSSION

Hilden et al.[8] conclude that a concentration of 10 ppm H_2S in solution leads to a highly defective surface film and, therefore, also to an increased oxidation rate. Hermansson and Eriksson also report much faster surface processes in the presence of sulfides. The catalytic effect of sulfides and sulfide scales on copper corrosion under oxidizing conditions has also been observed by others and has been subject to studies in the past; see e.g. [17] and also references therein. McNeil et al. have studied the adherence of sulfide layers produced by corrosion of copper alloys [18]. They exposed copper to synthetic seawater with oxygen contents ranging from < 0.02 mg/l to 7.00 mg/l and with sulfide concentrations ranging from 1 to 289 ppm. In all experiments except the ones with the lowest oxygen content, the sulfide was consumed during the course of the experiments (140 days). Hermansson and Eriksson [14] also lost the sulfide during their long-term exposures.

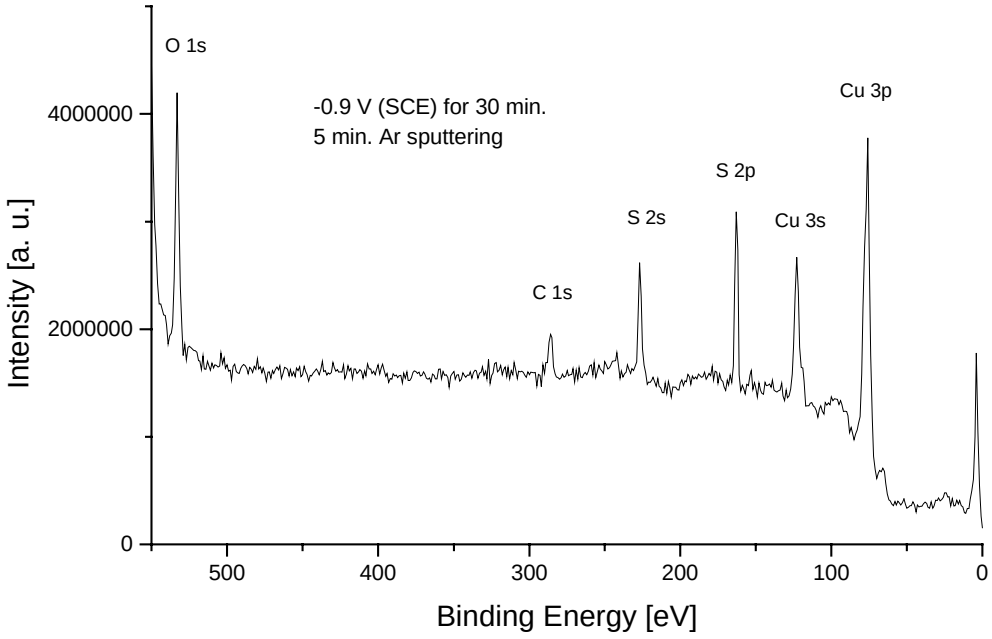

Figure 2. XPS spectrum of the binding energy range 0 – 550 eV of a copper coupon polarized at –0.9 V_{SCE} for 30 minutes after 5 minutes argon sputtering.

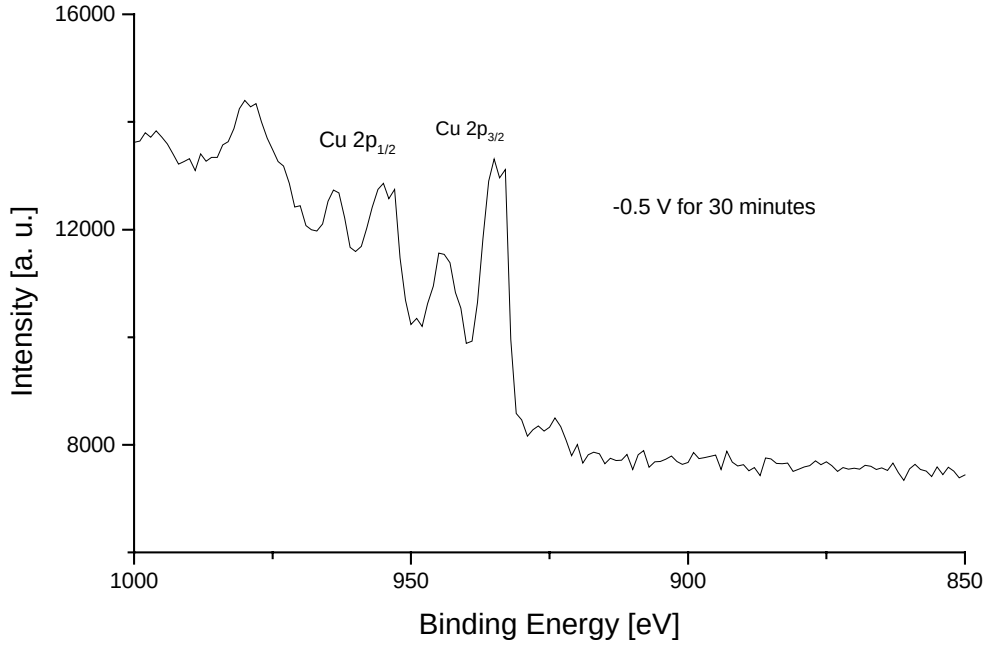

Figure 3. XPS spectrum of the Cu $2p_{1/2} - 2p_{3/2}$ region showing of a copper coupon polarized at – 0.5 V_{SCE} for 30 minutes in 1 ppm Na_2S before argon sputtering.

McNeil et al.[18] conclude that the corrosion products formed on copper in solutions containing high concentrations of dissolved sulfides and low oxygen concentrations are composed of adherent copper sulfides as predicted from the Pourbaix diagrams. In aerated solutions, the corrosion products tended to be chemically inhomogeneous. During the corrosion processes, oxidized minerals such as paratacamite ($Cu_2[OH]_3Cl$) form and may persist if the oxygen/sulfur ratio is favorable. Hermansson and Eriksson make similar observations [14]. In their experiment, massive corrosion products formed in the form of whiskers from the copper surface. Only trace amounts of sulfur were found in these whiskers. Instead, Hermansson and Eriksson proposed that copper oxide (CuO or Cu_2O), copper hydroxide ($Cu(OH)_2$), copper chloride-hydroxide ($CuCl_2 \cdot 3Cu(OH)_2$ *cf. atacamite/paratacamit)* or some combination of these phases probably constitutes the growing whisker. They conclude, however, that sulfide seem to be necessary for whisker mechanism to work.

These observations seem to be in line with what we have observed in this study. Only for very high sulfide concentrations and samples polarized at –0.9 V we could clearly observe adherent

sulfides as corrosion products. This is also in agreement with the observations of Vasquez Moll et al. [9]. From voltammograms of copper electrodes in 0.01 mol/dm^2 Na_2S they observed an anodic peak at –0.94 V_{SCE}, which was related to the formation of an adherent black film on the electrode. At potentials more positive than –0.74 V_{SCE} this adherent film breaks down and is replaced by poorly adherent corrosion products. At potentials greater than –0.5 V_{SCE}, they observed copper oxide electroformation. Our observations are consistent with those of Vasquez Moll et al. For the sample polarized at –0.7 V_{SCE} we could observe only weak indications of surface sulfide. The samples polarized at –0.5 V_{SCE} we observed only copper oxides, with a outermost surface layer of a Cu(II) corrosion product. This is line with the commonly observed duplex corrosion product layer on copper with an inner layer of Cu_2O and an outer layer of a Cu(II) salt. The composition of this outer layer depends on the solution chemistry; in seawater it is often paratacamite ($Cu_2[OH]_3Cl$) (see above), while in water with lower chloride activity species such as CuO or, if high level of carbonate are present, malachite ($Cu_2CO_3(OH)_2$) may form.

ACKNOWLEDGEMENT

PROCOBRE-Chile contributed to the support of this research.

REFERENCES

1. L. Werme, *Design premises for canister for spent nuclear fuel*, Svensk Kärnbränslehantering AB, Stockholm, Sweden, Technical Report TR-98-08 (1998).
2. H. Raiko and J-P. Salo, *Design report of the canister for nuclear fuel disposal*, Posiva Oy, Helsinki, Finland, Report Posiva-96-13 (1996).
3. Svensk Kärnbränslehantering AB, *SR 97: Waste, repository design and sites. Background report to SR 97*, Svensk Kärnbränslehantering AB, Stockholm, Sweden, Technical Report TR-99-08 (1999).
4. I. Puigdomènech, L. Trotignon, S. Kotelnikova, K. Pedersen, L. Griffault, V. Michaud, J-E. Lartigues, K. Hama, H. Yoshida, J.M. West, K. Bateman, A.E. Milodowski, S.A. Banwart, J. Rivas Perez and E-L. Tullborg, in: *Scientific Basis for Nuclear Waste Management XXIII*, edited by R.W. Smith and D.W. Shoesmith, (Mater. Res. Soc. Proc. **608**, Warrendale, PA, 2000) pp. 179-184.
5. K. Pedersen, M. Motamedi, O. Karnland and T. Sandén, *J. Appl. Microbiol.* **89**, 1038-1047 (2000).
6. K. Pedersen, M. Motamedi, O. Karnland and T. Sandén, *Eng. Geol.* **58**, 149-161 (2000).
7. I. Puigdomènech and C. Taxén, *Thermodynamic data for copper. Implications for the corrosion of copper under repository conditions*, Svensk Kärnbränslehantering AB, Stockholm, Sweden, Technical Report TR-00-13 (1998).
8. M.R. Gennero de Chialvo and A.J. Arvia, *J. Appl. Electrochem.* **15**, 685-696 (1985).
9. D. Vasquez Moll, M.R.G. de Chialvo, R.C. Salvarezza and A.J. Arvia, *Electrochimica Acta* **30**, 1011-1016 (1985).
10. D.D MacDonald, B.C. Syrett and S.S. Wing, *Corrosion* **35**, 367-378 (1979).
11. E.D. Mor, A.M. Beccaria, *British Corrosion Journal* **10**, 33-38 (1975).
12. J.N. Alhajji and M.R. Reda, *J. Electrochem. Soc.* **141**, 1432-1439 (1994).

13. J. Hilden, T. Laitinen, K. Mäkelä, T. Saario and M. Bojinov, *Surface films and corrosion of copper*, Statens Kärnkraftsinspektion, Stockholm, Sweden, SKI Report 99:27 (1999).
14. H-P. Hermansson and S. Eriksson, *Corrosion of the copper canister in the repository environment*, Statens Kärnkraftsinspektion, Stockholm, Sweden, SKI Report 99:52 (1999).
15. F. King and S. Stroes-Gascoyne In Proc. 1995 Int. Conf. *on Microbially Influenced Corrosion*, NACE International and American Welding Society (Houston, TX and Miami, FL,), 35/1-35/14 (1995).
16. I.S. Escobar, E. Silva, C. Silva and A. Ubal, in: Proc. *Copper 99-Cobre 99 International Conference, Vol. 1,* edited by G.A. Eltringham, N.L. Piret and M. Sahoo, (The Minerals, Metals & Materials Society, Warrendale, PA, 1999) pp. 371-386.
17. S. Jacobs and M. Edwards, *Wat. Res.* **34**, 2798-2808 (2000).
18. M.B. McNeil, A.L. Amos and T.L. Woods, *Corrosion*, **49**, 755-758 (1993).

SEGREGATION OF 3*sp* IMPURITIES TO $\Sigma = 5(310)$ TILT GRAIN BOUNDARY IN COPPER

P. A. KORZHAVYI, B. JOHANSSON,
Applied Materials Physics, Department of Materials Science and Engineering,
Royal Institute of Technology, SE-100 44 Stockholm, Sweden;

A. Y. LOZOVOI, and A. ALAVI
Atomistic Simulation Group, School of Mathematics and Physics,
The Queen's University of Belfast, Belfast BT7 1NN, Northern Ireland, U.K.;
Chemistry Department, University of Cambridge, Lensfield Road,
Cambridge CB2 1EW, U. K.

ABSTRACT

On the basis of the first principles density-functional calculations, the equilibrium atomic structure of the $\Sigma = 5(310)[001]$ symmetrical tilt grain boundary in Cu is obtained, and the segregation energies of Al, Si, P, and S impurities to the grain boundary are estimated.

INTRODUCTION

Because of its excellent corrosion resistance, copper is the material of choice for the outer shell of nuclear waste storage canisters. The mechanical properties of dilute copper alloys are very sensitive to the presence of small amount of impurities such as sulfur and phosphorous, due to segregation of these impurities towards the grain boundaries. Grain boundary (GB) segregation of phosphorus in copper may also contribute to the effect of stress corrosion cracking of phosphorous-deoxidized copper in ammoniacal environments [1]. Therefore, the main purpose of the present work is to obtain a theoretical estimate of the segregation tendency of impurities to a representative grain boundary in pure copper.

Most of the grain boundaries in Cu have coincidence site lattice (CSL) orientations [2]. The energies of $\Sigma = 3$ tilt grain boundaries may vary from 0.1 to 1.2 J/m^2 depending on the tilt axis and inclination angle [3,4]. It is believed that the energy of a random grain boundary becomes rather independent of grain misorientation at high misorientation angles [5]. The following estimates of the energies for these high-angle GBs were obtained: 0.5 – 0.6 J/m^2 (Gjostein and Rinnes [6]), 0.59 J/m^2 (Hillard *et al.* [7]), 0.6 – 0.8 J/m^2 (Wolf [8]). A considerable amount of impurity segregation is expected to occur at high-energy random grain boundaries, whereas segregation to low-energy CSL grain boundaries (like $\Sigma = 3$ symmetrical twin boundary) must be rather weak [9].

In the present work we perform a systematic study of the segregation energy of 3*sp* impurities (Al, Si, P, and S) to the $\Sigma = 5(310)[001]$ symmetrical tilt grain boundary in Cu using *ab initio* pseudopotential calculations based on density functional theory. The $\Sigma = 5(310)[001]$ GB is a CSL grain boundary and, therefore, can be modeled using a reasonably large supercell. On the other hand, it has a relatively high energy, of the same order as the energy of a random GB. Experimentally, the $\Sigma = 5(310)[001]$ GB in Cu-based alloys has been found to be susceptible to dynamic embrittlement [10], as well as to stress corrosion cracking [11].

METHODOLOGY

Terminology and definitions

Let us consider the grain boundary being in equilibrium with the bulk crystal on the both sides, at certain pressure p and temperature T. The bulk crystal serves, in particular,

as a reservoir of impurity atoms, which exist there in a small concentration (such that we could neglect any interaction between them) and which can segregate to the GB.

If the Gibbs free energy G of a piece of material containing the grain boundary is known, the excess Gibbs free energy of the grain boundary γ can be found as [12]:

$$\gamma = \frac{1}{A}(G - \sum_i \mu_i N_i) \quad , \tag{1}$$

where A is the GB area within the chosen box, N_i is the number of atoms of species i that the box contains, and μ_i is the chemical potential of species i.

In the simplest case when no impurities are present in the system (pure GB), Eq. (1) simply reduces to:

$$\gamma_0 = \frac{1}{A}(G_{pure} - \mu_0 N_s) \quad , \tag{2}$$

where subscript "0" refers to the host species (Cu), and N_s is the number of atoms in the slab representing the GB. The *equilibrium structure* of the pure GB is then the result of minimization of γ_0 with respect to internal parameters: N_s and the atomic coordinates. Hereafter, we consider only the $p = 0$ case, and assume the temperature to be low enough to neglect any vibrational entropy contribution to the Gibbs free energy, as well as the thermal expansion effects. Thus, the Gibbs free energy becomes the total energy at $T = 0$ as given by *ab initio* calculations.

The second quantity which is the matter of our concern here, the impurity segregation energy, is quite well known. Therefore we provide just a short comment, referring the reader to Ref. [13] for instance, for detailed discussion.

In equilibrium, the chemical potentials of all species, and impurities in particular, are constant throughout the system. That implies that transferring an infinitesimal amount of atoms to or from the GB does not change the Gibbs free energy of the whole system. In terms of energetic balance, the energy change due to the transfer is exactly compensated by other contributions to the Gibbs free energy, mainly coming from the change of the configurational entropy. To characterize the equilibrium in a rigorous way, one should calculate the equilibrium segregation profile of the impurity near the GB as a function of temperature; consideration of that type (see, e.g., Refs. [14–17]) is however beyond the scope of the present paper.

Instead, we characterize the *tendency* of a given impurity to segregate to the GB by taking only the energy change from the above balance, which would formally correspond to considering the difference between the GB free energy with and without an impurity atom at $T = 0$. Replacing therefore in Eqs. (1) and (2) the Gibbs free energy G by the total energy E, and assuming that the number of impurity atoms at the GB is still small enough to neglect any interaction between them, we arrive at the following expression for the energy change *per impurity atom*, or segregation energy:

$$\Delta\varepsilon_i = E_i - E_{pure} - (\mu_i - \mu_0) \quad , \tag{3}$$

assuming that only substitutional type of segregation occurs; and

$$\Delta\varepsilon_i = E_i - E_{pure} - \mu_i \tag{4}$$

for the interstitial impurity (per chance, we shall not consider the second type of segregation in the current study). We denote via E_i the energy of the GB with one host atom replaced by the atom of impurity i, Eq. (3), or the energy of the GB having an impurity atom in the interstitial position Eq. (4). Eq. (3) coincides with the formula used in Ref. [18] to calculate the heat of Ga segregation to the $\Sigma = 11(113)$ GB of aluminum. It could be also verified

that the definition (3) represents a finite difference analog of the formulae giving the *surface* segregation energies (see, e.g., Eqs.(26)-(28) in Ref. [13]). Alternatively, one could arrive at Eqs. (3)-(4) by employing the formalism describing the thermodynamics of excesses on grain boundaries and other types of interfaces [19].

Supercell geometry

The atomic structure of the $\Sigma = 5(310)[001]$ symmetrical tilt grain boundary (GB) in the fcc Cu was modeled using an orthorhombic unit cell (schematically shown in Fig. 1) with the unit cell dimensions $\mathbf{a} = (a_0/2)[1\bar{3}0]_{\text{fcc}}$ and $\mathbf{c} = a_0[001]_{\text{fcc}}$ where the equilibrium lattice constant of fcc Cu ($a_0 = 3.605$ Å) was taken from the bulk calculation. In the ideal CSL geometry, the supercell contained 32 atomic $(310)_{\text{fcc}}$ planes perpendicular to axis **b**. This third dimension of the supercell was then considered as a variable parameter which had to be found from the calculations of total energy as a function of b.

The unit cell shown in Fig. 1 contains two grain boundaries: one at $y = 0$ and the other, with the opposite orientation, at $y = \frac{1}{2}$. There are 30 atomic and 2 interstitial sites (10 inequivalent positions) in the unit cell. The impurity atoms and vacancies were considered at symmetric positions in the grain boundary core (positions 1 and 9). Position 10 is an interstitial site at the GB and it was kept unoccupied (except for one case in which the energy of an interstitial Cu atom was calculated).

In order to minimize the systematic errors due to the numerical integrations in reciprocal space, the bulk-like atomic configurations were considered within the orthorhombic, 30-atom supercell based on the fcc structure, with the lattice parameters given by $\mathbf{a} = (a_0/2)[1\bar{3}0]_{\text{fcc}}$, $\mathbf{b} = (3a_0/2)[310]_{\text{fcc}}$, and $\mathbf{c} = a_0[001]_{\text{fcc}}$. As one can see, the closest separation distance between the impurities was $a_0[001]$ in both the GB and bulk supercells. This choice of the bulk supercell allowed us to eliminate, at least partially, the systematic error due to the impurity-impurity interaction.

Details of calculations

Our calculations were performed using the plane wave pseudopotential method within the framework of the finite-temperature density functional theory [20], using the local density approximation [21]. For the Brillouin zone integration, the $4 \times 2 \times 6$ Monkhorst-Pack mesh was employed. A soft kinetic-energy-filtered pseudopotential [22] represented copper in our study, and we used the Troullier-Martins pseudopotentials [23] for the other species. The chosen pseudopotentials were checked against full-electron calculations of hypothetical Cu_3X $L1_2$ type compounds (X = Cu, Al, Si, P, and S), and yielded similar equations of state. The electronic orbitals were expanded up to a cutoff energy of 60 Ry.

In all considered configurations, the atomic positions were optimized until the maximum force component dropped below 2 mRy/a.u. (the atoms 2, 3, 5, 7, and 8 on Fig. 1 represented the bulk and thus were kept fixed). An effective strategy was to perform the local atomic displacements first at a smaller cutoff (40 Ry), and then take the relaxed configuration to start another relaxation at 60 Ry cutoff: in most cases only a few additional iterations were required, and sometimes the configuration turned out to be already final.

Optimization of the supercell parameter b turned out to be computationally rather expensive. In a bulk calculation of similar type, lots of effort can be saved if the atomic positions, obtained at one lattice parameter, are rescaled to prepare the starting configuration at some other lattice parameter. This did not help in the case of supercells containing the grain boundaries, because upon changing b we had to keep relative distances between the fixed bulk-like atoms, thus the "stretch" of the supercell was not uniform.

On the other hand, it turned out that the relaxation of the supercell lattice parameter b did not significantly affect the segregation energies. Therefore, we have performed the relaxation of b for all GBs of the pure Cu, but only for selected impurity segregation cases

(see Table II), in which further clarification was needed. This relaxation changed the result qualitatively only for the vacancy segregation, in which case the segregation energy was small, and the relaxation of the b parameter was the largest.

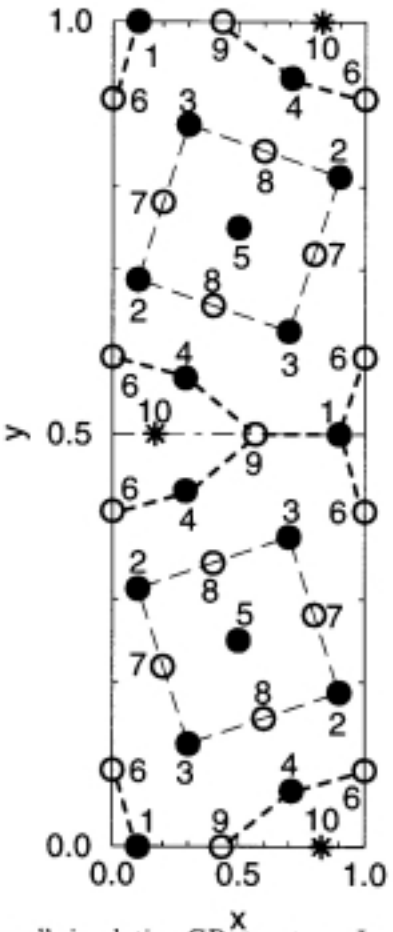

FIG. 1. Orthorhombic supercell simulating GB structure. Inequivalent positions are labeled by different numbers. The full and open symbols correspond to levels z=0 and z=1/2, respectively. The asterisks indicate the positions of the interstitial sites. The tilted squares show the contours of the fcc unit cells. The dashed lines indicate the GB core regions.

RESULTS AND DISCUSSION

Equilibrium structure of the pure GB

In determining the equilibrium atomic structure of the $\Sigma = 5(310)[001]$ symmetrical tilt GB in fcc Cu, three different models having different number of atoms N_s were considered, and their excess energies γ_0, Eq. (2), were compared. In the first model (GB1), all the atomic positions shown on Fig. 1 were occupied and the interstitial sites (positions 10) were empty. The second model of the GB core (GB2) was the supercell with additional Cu atoms in positions 10. In the third model, positions 1 and 10 were empty (GB3).

The minimal calculated γ_0, see Table I, corresponds to the first GB model. Therefore we identify the GB1 as the equilibrium grain boundary. Consequently, the GBs given by models 2 and 3 represent GB with an interstitial atom and with a vacancy, respectively. In Table I, we also list the effective GB width, Δw, which is defined as the excess volume associated with the grain boundary (per GB area); for convenience we express it in units of the $(310)_{fcc}$

interplanar spacing, $d_{310} = a_0/2\sqrt{10} \simeq 0.570$ Å:

$$\Delta w = (b - b_0)/2d_{310} \quad ,$$

where $b_0 = N_s d_{310}$ is the size of the fcc-based supercell (without grain boundaries) containing the same number of atoms, N_s. As it may be expected, the effective GB width increases upon the introduction of vacancies and decreases upon the introduction of interstitial atoms into the GB core.

TABLE I. Comparison of the different models simulating the pure $\Sigma = 5(310)[001]$ GB in Cu. For each considered model, the Table lists the number of atoms within the supercell N_s, the effective width of the GB Δw in units of $d_{310} \simeq 0.570$ Å(see text for definitions), and the excess grain boundary energy γ_0, Eq. (2). The lowest energy grain boundary (GB1) is taken as an equilibrium GB.

GB model	N_s	Δw	γ_0, J/m^2	Comments
GB1	30	0.669	0.76	Equilibrium GB
GB2	32	0.311	1.19	GB with an interstitial atom
GB3	28	1.103	1.55	GB with a vacancy

The relaxed structure of the core of the equilibrium GB was similar to that obtained in the very recent embedded atom simulations [24]. That was quite an encouraging result, as Sørensen and co-workers [24] checked the equilibrium structure against a translation of the grains parallel to each other, which we did not attempt. Also such agreement indicated that the thickness of the slab representing the GB in our study was sufficient to reproduce the correct equilibrium structure. The energy of the equilibrium GB reported in [24], 0.888 J/m^2, was close to that obtained in our study.

Segregation energies

The calculated segregation energies of Al, Si, P, and S impurities and also of vacancies to symmetrical positions in the GB core (positions 1 and 9) are listed in Table II. Negative sign of the segregation energy corresponds to segregation, positive sign corresponds to anti-segregation of an impurity.

The aluminum impurity is found to antisegregate from the grain boundary. All the other considered impurities and also vacancies are found to prefer position 1 to position 9 in the GB core. The segregation tendency of impurities increases upon going from Si to S. One should keep in mind that the calculated absolute values of the segregation energy given in Table II correspond to a CSL grain boundary, namely, the $\Sigma = 5(310)[001]$. Therefore, they must be systematically lower than the absolute values of the impurity segregation energy to random grain boundaries [9].

Let us now compare the calculated segregation energies of two most important impurities, P and S, with other estimates that can be made on the basis of available experimental and theoretical data. The simplest (but also rather rough) estimate of the free energy of impurity segregation to a random, high-angle GB may be obtained from the difference in slopes between the *liquidus* and *solidus* lines on the equilibrium phase diagram, i.e. as

$$\frac{dC_L/dT}{dC_S/dT} = \exp\left(-\Delta g_i/k_B T\right) \quad ,$$

where C_L and C_S are the *liquidus* and the *solidus* concentrations, respectively, and k_B is the Boltzmann's constant. From the phase diagrams of Ref. [25] one obtains the following

estimates for the energy of phosphorous, $\Delta g_i = -0.23$ eV, or sulfur, $\Delta g_i = -0.48$ eV, segregation to a random GB in Cu. These estimates turn out to be very close to the corresponding vacancy-impurity interaction energies in copper calculated in Ref. [26], $E_{vac-P} = -0.28$ eV and $E_{vac-S} = -0.46$ eV. They are also in reasonable agreement with the results obtained in the present study.

TABLE II. Calculated segregation energies $\Delta\varepsilon_i$ of $3sp$ impurities and vacancies to symmetric positions in the core of the $\Sigma = 5(310)[001]$ GB in Cu. Numbers without brackets were obtained by inserting the impurity/vacancy in the equilibrium GB of pure copper and subsequent relaxation of atomic positions, the numbers in brackets were calculated having additionally adjusted the supercell size b.

i	$\Delta\varepsilon_i$, eV/atom	
	Position 1	Position 9
Al	+0.297	+0.152
		(+0.151)
Si	−0.029	+0.368
P	−0.142	+0.305
S	−0.279	−0.043
	(−0.288)	
vac	+0.078	+0.371
	(−0.056)	

CONCLUSIONS

We find that the segregation tendency increases when going from aluminum to sulfur. Aluminum is found to anti-segregate from the GB, Si has a very small segregation energy, whereas in the case of P and S we obtain moderate and strong segregation tendency, respectively. The calculations show that position 1 may be a preferable site for GB segregation of P and S impurities in Cu, and also for trapping vacancies.

ACKNOWLEDGMENTS

This work is supported by SKB AB, The Swedish Nuclear Fuel and Waste Management Company and by the EPSRC via Grant L08380. The Centre for Supercomputing in Ireland is acknowledged for computer resources on the IBM SP2.

REFERENCES

[1] S. Sato and K. Nagata, Journal of Japan Copper and Brass Research Association **11**, 202 (1978).
[2] M. P. Burton-Guillen, J. G. Cabanas-Moreno, and J. R. Weertman, Scripta Metall. Mater. **24**, 991 (1990).
[3] F. Ernst, M. W. Finnis, A. Koch, C. Schmidt, B. Straumal, and W. Gust, Z. Metallkd. **87**, 911 (1996).
[4] C. Schmidt, M. W. Finnis, F. Ernst, and V. Vitek, Philos. Mag. A **77**, 1161 (1998).
[5] T. Surholt and Chr. Herzig, Acta Mater. **45**, 3817 (1997).
[6] N. A. Gjostein and F. N. Rinnes, Acta Metall. **7**, 319 (1959).
[7] J. E. Hillard, M. Cohen, and B. L. Averbach, Acta Metall. **8**, 26 (1960).

[8] D. Wolf, Acta Metall. Mater. **38**, 791 (1990).
[9] H. Gleiter and B. Chalmers, *High-Angle Grain Boundaries*, (Pergamon Press, Oxford, 1972).
[10] R. C. Muthiah, J. A. Pfaendtner, S. Ishikawa, and C. J. McMahon Jr, Acta Mater. **47**, 2797 (1999).
[11] T. Mimaki, H. Ando, H. Miyamoto, Y. Kaneko, and S. Hashimoto, Materials Science Forum **294-296**, 169 (1999).
[12] J. W. Cahn, in: *Interfacial Segregation*, Edited by W. C. Johnson and J. M. Blakely (American Society for Metals, Ohio 1977).
[13] A. V. Ruban and H. L. Skriver, Comput. Mater. Sci. **15**, 119 (1999).
[14] V. Drchal, A. Pasturel, R. Monnier, J. Kudrnovský, and P. Weinberger, Comput. Mater. Sci. **15**, 144 (1999).
[15] I. A. Abrikosov and H. L. Skriver, Phys. Rev. B **47**, 16532 (1993).
[16] I. A. Abrikosov, A. V. Ruban, H. L. Skriver, and B. Johansson, Phys. Rev. B **50**, 2039 (1994).
[17] A. V. Ruban, H. L. Skriver, and Nørskov, Phys. Rev. B **59**, 15990 (1999).
[18] D. I. Thomson, V. Heine, M. C. Payne, N. Marzari, and M. W. Finnis, Acta Materialia, **48**, 3623, (2000).
[19] M. W. Finnis, Phys. stat. sol. (a) **166** (1998) 397.
[20] A. Alavi, J. Kohanoff, M. Parrinello, and D. Frenkel, Phys. Rev. Lett. **73**, 2599 (1994).
[21] D. M. Ceperley and B. J. Alder, Phys. Rev. Lett. **45**, 566 (1980); J. P. Perdew and A. Zunger, Phys. Rev. B **23**, 5048 (1981).
[22] M. H. Lee, Ph.D. thesis, University of Cambridge, 1995.
[23] N. Troullier and J. L. Martins, Phys. Rev. B **43**, 1993 (1991).
[24] M. R. Sørensen, Y. Mishin, and A. F. Voter, Phys. Rev. B, **62**, 3658 (2000).
[25] *Binary Alloy Phase Diagrams*, Second Edition, edited by T. B. Massalski, (ASM International, 1990)
[26] P. A. Korzhavyi, I. A. Abrikosov, and B. Johansson, Acta Mater. **47**, 1417 (1999).

Influence of phosphorous on creep in pure copper

Henrik C. M. Andersson, Facredin Seitisleam, Rolf Sandström
Swedish Institute for Metals Research
Drottning Kristinas v. 48, S-114 28 Stockholm, SWEDEN

ABSTRACT

Spent nuclear fuel in Sweden is planned to be disposed of by encapsulation in double-walled canisters consisting of iron and copper, respectively, and placed deep in the bedrock. The main function of the outer copper canister is to provide corrosion resistance and the gap between the copper and the iron canister is initially 1 – 2 mm. When the canister is exposed to a slowly increasing external pressure this gap will close by creep since the temperature is estimated to 80-90 °C during the first 200 years. The aim of this project has been to investigate the creep behaviour of copper with different phosphorous content and assess the suitability as a canister material.
Uniaxial creep tests have been performed at 175 °C for extruded oxygen-free copper and the effect of different contents of phosphorous has been investigated. Copper with <1 ppm phosphorous content showed significantly lower creep life and ductility than batches with higher P content. An increase of the P content to 29 ppm increased the creep life and ductility, but a further increase did not affect the properties. Master curves for extrapolation are provided for creep rupture as well as for 5% and 10% creep strain.

INTRODUCTION

In Swedish spent nuclear fuel is planned to be disposed of by encapsulating in double walled canisters and buried 500 m deep in bedrock. The canisters will consist of an inner load bearing shell of iron, and an outer corrosion protective shell made of copper [1]. The method considered at the moment for the manufacturing of the copper canisters is extrusion [2]. Trial production performed has demonstrated it to be a feasible method. The temperature of the canisters due to the nuclear reactions within the spent fuel is estimated to be about 80-90 °C during the first 100-200 years in the repository, which will then decrease to about 15 °C during the first couple of thousand years [1]. It is during the high temperature period that the gap between the inner and outer shell of the canister is expected to close by creep due to external hydrostatic pressure. The maximum creep deformation of the copper has been estimated to 4%. It is important that the copper has adequate creep ductility to avoid failure of the copper canister.
Previously the creep properties of pure coppers have been studied extensively. Oxygen-free copper with about 50 ppm phosphorous (Cu-OFP) is covered in three reports [3, 4, 5]. A review of the creep properties of oxygen-free high conductivity copper (Cu-OF) is given in [6]. Of the two materials the Cu-OFP exhibited significantly higher creep strength and ductility.
The aim of this work is to study the effect of phosphorus content on the creep properties of pure copper.

EXPERIMENTAL

The extruded material was supplied by Outokumpu Poricopper OY, Finland and the composition and grain size can be found in Table 1, and the microstructure in Figure 1. The materials are

designated CuP0, CuP30, CuP60 and CuP105 with the number indicating the phosphorous content in ppm. As can be seen from the figure the microstructure is largely similar with about the same grain size and twinning density. Tensile properties and the hardness of the batches at room temperatures are listed in Table 2. These properties are very similar for the different batches. The materials follow essentially the UNS specifications of C10100 (99.99% Cu), C10300 (99.95% Cu+10-50 ppm P), and C10800 (99.95% Cu+50-120 ppm P).

Table 1 Material data for the extruded copper.

Test series	P (ppm)	Grain size (µm)	S (ppm)	H_2 (ppm)	O_2 (ppm)	$R_{p0.2}$ (MPa)	R_m (MPa)	Elong. (%)	Hardness (HV)
CuP0	< 1	300	6	< 0.5	1.1	62	228	45	55
CuP30	29	450	6	< 0.5	1.2	n/a	n/a	n/a	53
CuP60	58	350	6	< 0.5	1.1	52	225	45	55
CuP105	106	450	5	< 0.5	1.1	51	224	46	n/a

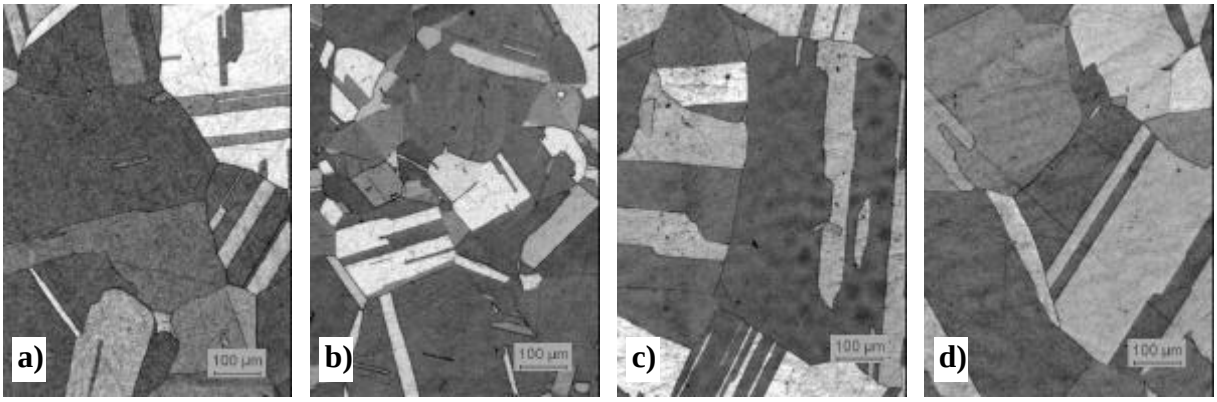

Figure 1. Microstructure in the material before creep testing. a) CuP0, b) CuP30, c) CuP60, d) CuP105. For material data see Table 1. LOM, 50x

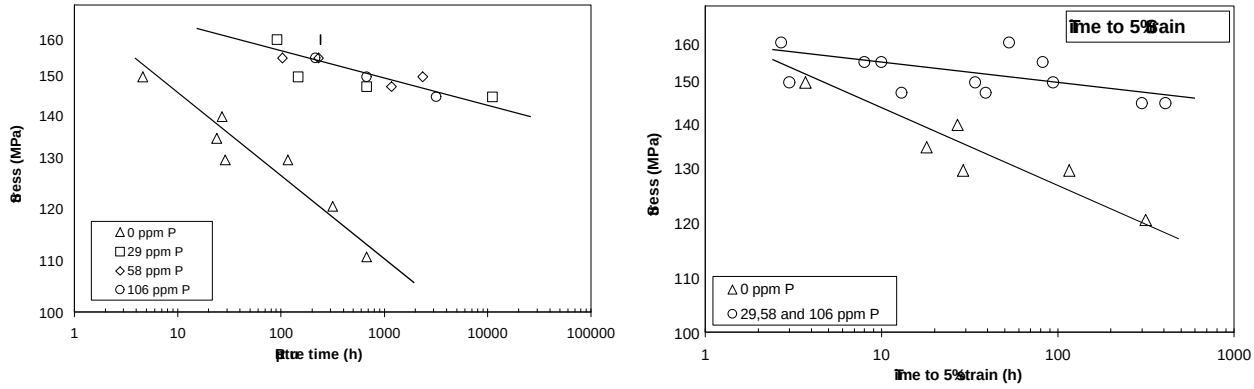

a) b)

Figure 2. a) Stress versus rupture time, b) Stress versus time to 5% creep strain.

RESULTS

Stress – rupture plots can be found in Figure 2a and time to 5% in Figure 2b. Significantly lower creep rupture strengths was found in the material with the lowest phosphorous content (<1 ppm P, CuP0). The rupture times for this material was up to two orders of magnitude lower at the same stress.
The minimum creep rate of a material $\dot{\varepsilon}_{ss}$ can be expressed by the Norton equation (1).

$$\dot{\varepsilon}_{ss} = B\sigma^n \qquad (1)$$

where B and n are constants and σ the stress. Applied to the testing performed in this work high values of the Norton exponent, n, was found. This is shown in Figure 3 where the exponent for the material with the lowest phosphorous content has been estimated to 21. All of the other tests can be condensed to a Norton exponent of 34. This shows that the test temperature is well inside the power law break-down area, and since the capsules are to operate at these stress levels the results are relevant. In Figure 4 the creep rupture strain properties is given. The material with the lowest phosphorous content exhibits the lowest ductility properties with elongation lower than 10% whereas the other materials with higher phosphorous content all have rupture strains of about 30%.
Cavities and microcracks are formed throughout the material with the lowest phosphorous content (<1 ppm P, CuP0) and wedge cracks can be found at triple points. Small, sharp microcracks (see Figure 5a) are present on the surface of the specimen, which has a facetted appearance, most likely the result of grain boundary sliding. No significant plastic deformation was observed close to the fracture.
In the material with a higher P content a shift towards more plastic deformation is evident. Both the materials with 29 ppm P (CuP30) and the material with 58 ppm P (CuP60) exhibit more microcracks without the preceeding cavity formation. In the 58 ppm P material, these microcracks can be found along the whole gauge length, see Figure 5b.

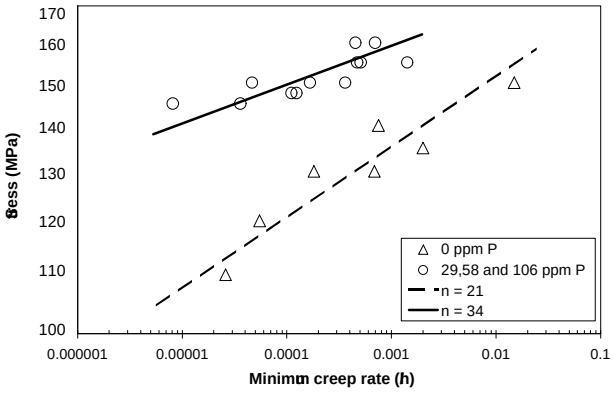

Figure 3. Norton plot.

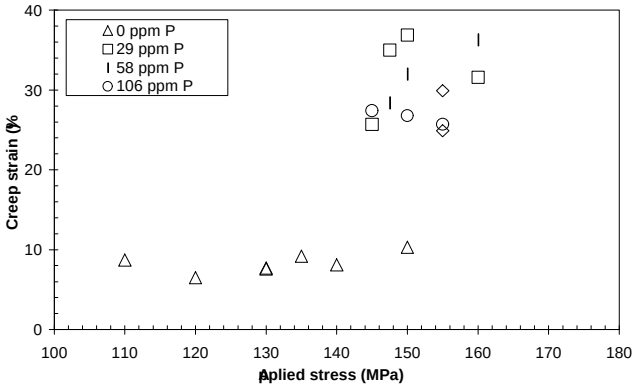

Figure 4. Creep rupture strain versus stress.

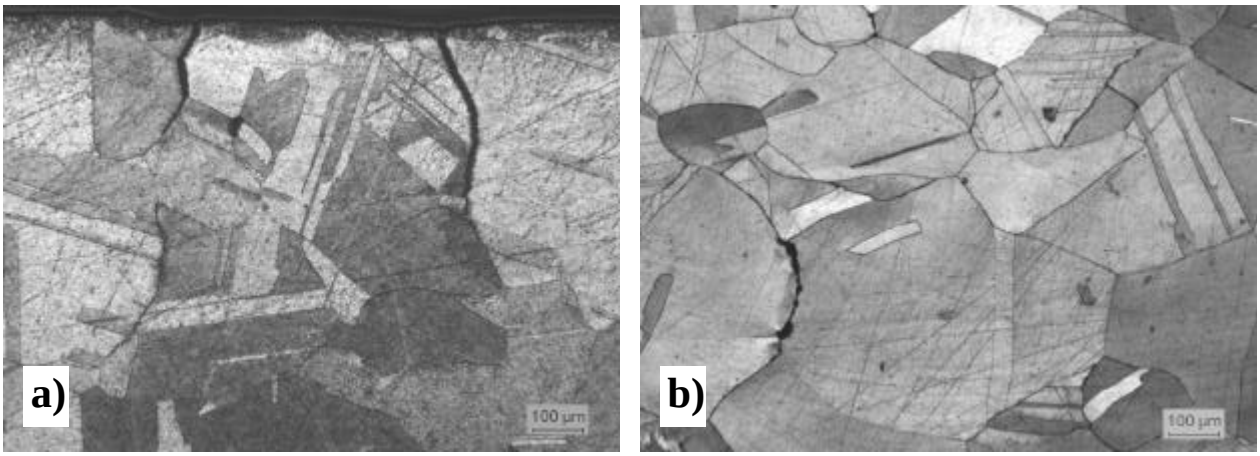

Figure 5. a) Microcracks starting at the surface 50 mm from the fracture in a specimen with <1 ppm P (CuP0). b) Microcracks formed by linking of cavities 50 mm from fracture in a specimen with 58 ppm phosphorous (CuP60).

Compared to the specimens with less phosphorous content the specimens with the highest phosphorous content (CuP105) show an even more marked reduction of both the cavity and the microcrack density. The plastic deformation of the material close to the fracture is large and few, if any, microcracks can be seen at a distance from the fracture.

EXTRAPOLATION OF THE CREEP RUPTURE DATA

Data from three of the materials tested in the present work together with one additional material with slightly higher sulphur content has been used for extrapolation. This extra material was tested at the same time and with the same test conditions as the others. Together with previously determined results for CU-OFP batches [3, 5] extrapolation of the results was performed using methods discussed in [7].
The Larson-Miller time temperature parameter

$$P_{LM} = T(\log t + C_{LM}) \qquad (2)$$

where T is the temperature in K, t the time in h, and C_{LM} is a constant, has been used. A second order polynomial in P_{LM} has been fitted to the data at the same time as the value of C_{LM} was assessed. The extrapolation was performed in a log stress – log P_{LM} environment. The resulting master curve is given in Figure 8, with the new data found at $P_{LM} < 6300$. Some data points in this range are from previous investigations. Extrapolation to 200 years at 75 and 100℃, the expected exposure in the repository, corresponds to P_{LM} values of 5800 and 6210 respectively, i.e. in the range of the new data. Corresponding rupture strengths is in the interval 135 to 155 MPa.
Extrapolation for the stresses to give 5 and 10% creep strain has also been carried out. The resulting master curves are also shown in Figure 6. Extrapolation to 200 years at 75 and 100℃ gives stresses in the range 115 to 130 MPa and 130 to 145 MPa for 5 and 10% creep strain respectively.

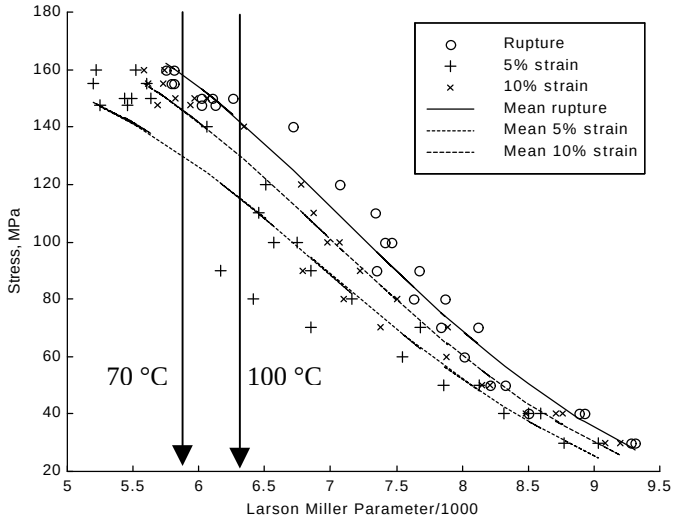

Figure 6. Master curve for rupture, 5 and 10% strain extrapolation. Stress versus the Larson-Miller parameter. The estimated stresses giving rupture and 5 and 10% creep strain after 200 years at 75 and 100℃ are marked with arrows.

DISCUSSION

The addition of 30-110 ppm P to pure copper reduces the creep rate and increases the rupture life dramatically. It is known that phosphorous reduces the rates of the softening processes recovery and recrystallization of pure copper [8]. Climb rates of dislocations and the migration rates of grain boundaries are much reduced due to solute-drag, see for example [9], yielding a lower creep rate. Recent estimates of the interaction energy between P-atoms and vacancies demonstrates that they develop a strong affinity which reduces the mobility of both dislocation cores and grain boundaries [10]. The mechanism giving the positive effect of P on the creep ductility is however still unknown. The creep rupture mechanism in materials with low P content is cavitation at grain boundaries and subsequent formation of microcracks by linking. In [6] it is shown that the segregation of sulphur in the form of Cu_2S to the grain boundaries is the probable cause of the low creep ductility of P-free copper. The proposal now is that S and P compete about the vacancy positions at the grain boundaries. P has a slightly higher affinity for vacancies and thus the brittle

grain boundary Cu_2S-phase cannot form yielding a higher creep ductility and greater creep rupture strength. The interaction between S, P and vacancies is more quantified in [10].
The Norton exponents observed in the present investigation is larger than those previously obtained for P containing materials. Values of about $n = 34$ have typically been found in the present work, which should be compared to $n = 5$ to 15 previous work at higher temperatures, [11]. The creep testing in those investigations was performed at 225 °C and above, as opposed to 175 °C in this investigation. Thus such a change is not surprising but rather demonstrates that there is a change in the deformation mechanism of P containing coppers around 200 °C. Above this temperature the deformation mechanism is power law creep and below power law break down takes place.

CONCLUSIONS

- An addition of 29 ppm phosphorous increased the creep strength and creep ductility significantly in comparison to P-free material.
- Further additions of phosphorous had little effect.
- Norton exponents are high for all tested materials (21 to 34)

ACKNOWLEDGEMENTS

This project was entirely funded by SKB AB. Outokumpu Poricopper OY supplied the test material and performed the grain size measurements and the tensile tests.

REFERENCES

1. L Werme, SKB Technical Report R-98-08, Stockholm (1998).
2. C-G Andersson, SKB Technical Report TR-98-09, Stockholm (1998).
3. F. Seitisleam, P.J. Henderson, J. Lindblom, Swedish Institute for Metals Research, Report IM – 3327 (1996).
4. P.J. Henderson, International Seminar on Design and Manufacture of Copper Canisters for Nuclear Waste, Sollentuna, Sweden, April (1994).
5. P.J. Henderson, L. Werme, Materials and Nuclear Power, EUROMAT 96, Bournemouth, United Kingdom, October (1996).
6. P.J. Henderson, R. Sandström, Materials science and engineering, **A246** (1998).
7. R. Sandström, Journal of Testing and Evaluation, JTEVA, Vol. **27**, No. 1, January (1999).
8. W B Hutchinson, R K Ray, Metals Science. *1979*, 125-130.
9. K Pettersson, Materials Research Centre, Report TRITA-MAC-0594 (1996)
10. P.A. Korzhavyi, I.A. Abrikosov, B. Johansson, Acta mater., Vol **47**, No 5, pp. 1417-1424 (1999).
11. R Sandström, Expert system on creep in copper, under development (1999).

The Development of Advanced Welding Techniques for Sealing Nuclear Waste Canisters.

Claes-Göran Andersson, Svensk Kärnbränslehantering AB (SKB), Stockholm, Sweden;
Richard E. Andrews, TWI Ltd, Great Abington, Cambridge, United Kingdom.

1. The Swedish system for nuclear waste management.

Sweden has 11 nuclear reactors in operation at 4 different sites. These reactors produce about 40% of all electricity used in Sweden. By 2010 the current nuclear program will have produced approximately 8000 metric tons of spent nuclear fuel. In the last 25 years a comprehensive system for radioactive waste management has been developed. This system is owned and managed by The Swedish Nuclear Fuel and Waste Management Co, (SKB) and consists of a Central Interim Storage Facility for spent nuclear fuel (CLAB), an underground repository for radioactive operational waste (SFR) and a transport system for spent fuel and radioactive waste. SKB is owned by the Swedish nuclear power utilities.

The central interim storage (CLAB) is located near the Oskarshamn Nuclear Power Plant. In CLAB the fuel assemblies are stored in water pools located in a rock cavern, approximately 25 meters below ground level. After 30 to 40 years of interim storage the fuel will be encapsulated in corrosion resistant disposal canisters. Encapsulation of the fuel will take place in an Encapsulation Plant, which will be built as an extension to CLAB. After encapsulation, the fuel will be transported to a geological repository, where the canisters will be deposited at a depth of 500 to 700 meters in granitic rock surrounded by bentonite clay, see Fig. 1.

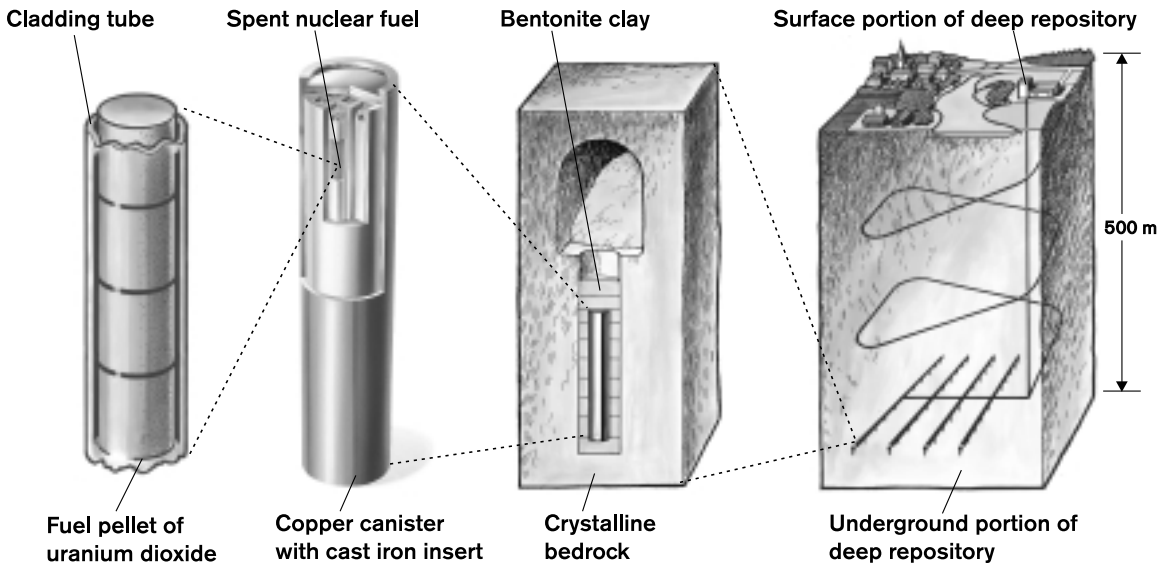

Figure 1. The multiple-barrier system in the repository: the nuclear fuel, the canister, the bentonite buffer and the bedrock.

The primary function of the canister in the deep repository is to isolate the spent fuel from the environment. As long as the canister is intact, all dispersal of radioactivity is prevented. The canister is designed to withstand all known corrosion processes so that it will remain intact in

the deep repository for at least 100,000 years. If the canister should nonetheless fail, the other barriers are supposed to retard and attenuate the dispersal of radionuclides to acceptable levels. The canister must also be able to withstand the mechanical loads anticipated in the deep repository. These are caused by the pressure exerted by the ground water and the swelling bentonite. Future ice ages or major rock movements can also give rise to mechanical stresses on the canister.

2. Canister design and fabrication methods.

The reference canister designed by SKB consists of an outer corrosion barrier of 50mm thick copper and a pressure-bearing insert of nodular iron, see Fig. 2. The canister holds either 12 BWR assemblies or 4 PWR assemblies.

Calculated Weight (kg):	
Copper Canister	7 400
Cast Insert	13 600
Fuel Assemblies (BWR)	3 600
In Total	24 600

Figure 2. Copper canister with nodular cast iron insert for BWR fuel.

As the result of extensive studies since the end of the 1970s copper has been chosen to satisfy the requirement on chemical resistance in the environment prevailing in the deep repository. The specified grade is equivalent to UNS 10100 (Cu OFE) or EN133/63:1994 Cu-OF1 with an addition of about 50ppm phosphorus to increase the materials creep ductility. In the current design the wall thickness of the copper is 50 mm but may be reduced to 30 mm.

In the last five years, fabrication trials with copper canisters and cast inserts have been conducted on a full scale by means of different methods. Full-size copper cylinders have been manufactured using three different methods, roll forming of tube halves that are welded together and seamless tubes produced by extrusion or pierce and draw processing. Copper lids and bottoms are machined from material that has been performed by forging. To complete an empty canister the bottoms are welded to the machined copper tubes and after that the insert is lowered down into the copper shell. To ensure the production of empty canisters, at a rate of

over 200 per year, SKB is designing a special Canister Factory. From this factory the canisters will be delivered to the encapsulation plant. After loading the canister with fuel assemblies the final sealing of the canister will take place in the encapsulation plant.

3. Welding and sealing techniques.

Extensive work programmes have been carried out in co-operation between SKB and TWI, on the development of welding techniques for the copper over-pack. So far all full scale welding of tube halves, welding of bottoms and lids have been performed by electron beam welding. To establish the technique for the sealing weld of the lid in the encapsulation plant a Reduced Pressure EBW-prototype equipment has been designed and installed in the Canister Laboratory located in Oskarshamn, see Fig. 3. In this laboratory the efforts will be concentrated on establishing the exact production route and technique that will be used when full-scale encapsulation starts.

Figure 3. The Canister Laboratory in Oskarshamn.

During the last years SKB and TWI have together also studied the possibility of using Friction Stir Welding (FSW) as an alternative to EBW for fabrication and sealing of copper canisters.

4. Electron Beam Welding.

In 1981 it was estimated that copper waste storage canisters should have a wall thickness of 200mm to provide sufficient corrosion resistance and adequate strength to survive intact for 100,000 years. The canister design consisted of a cylinder closed at either end using a sealing technique such as welding, that produced excellent joint integrity to combat localised corrosion.

However, thick section copper is not easy to weld due to its high thermal diffusivity and therefore the heat input into a weld interface needs to be high to overcome this effect. The only method in 1981 considered to be practical for this application was High Vacuum (HV) Electron Beam Welding (EBW) with its high absolute power and high power density capability. HVEBW is known as a fusion welding technique because components are joined together by solidification across the weld interface from the molten state. This results in a cast microstructure which can contain porosity and other associated weld flaws.

Using this technique TWI were able to demonstrate that a simulated canister to lid assembly with a wall thickness of 100mm could be joined at a low pressure of 5 x 10^{-3}mbar. However, for production welding it was not considered to be practical to pump a large chamber capable of containing a complete canister to such a low pressure. At this point effort moved towards improved electron beam gun design leading to higher power systems and the attractive capability of working at higher pressures. A process variant known as Reduced Pressure (RP) EBW operating at pressures from 0.1 to 100mbar was selected for lid to canister welding.

The RPEBW process produces narrow, deep penetration weld zones with rounded roots which greatly reduce the occurrence of weld root defects. An example of this type of weld zone is shown in Fig. 4.

Prototype RPEBW has been designed and built by TWI and installed at SKB's Canister Laboratory at Oskarshamn. The equipment is currently being used to produce circumferential closure welds, which are undergoing integrity assessment in terms of metallurgical and mechanical properties. Information generated will be incorporated into the results of an on-going feasibility study, which is aimed at approval of the preferred encapsulation process by 2004.

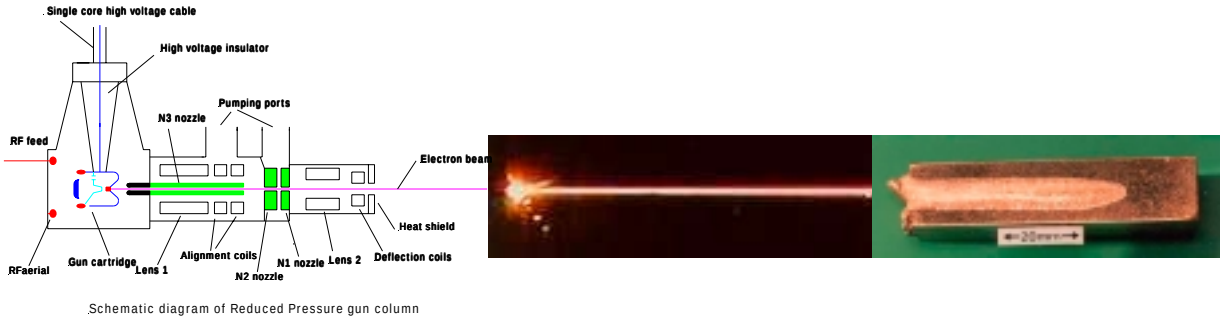

Figure 4. Schematic diagram of Reduced Pressure EBW gun column. RPEBW at 5mbar pressure, 200kV, 300mA, helium. Apparent beam diameter ~4mm. Unique round bottomed RPEBW fusion zone in copper.

5. Friction Stir Welding.

By the early 1990's the development of RPEBW was well advanced. However, in 1997 SKB also recognised that Friction Stir Welding (FSW), a new solid phase welding process, had the potential to be considered as an additional or complementary method for making complete circumferential canister closure welds.

In contrast to RPEBW, which is a fusion welding technique, FSW joints are produced at a temperature of 700-900°C, which is below the melting point of copper. The FSW technique

involves the translation of a rotating tool along the joint between two abutted copper plates as shown in Fig. 5.

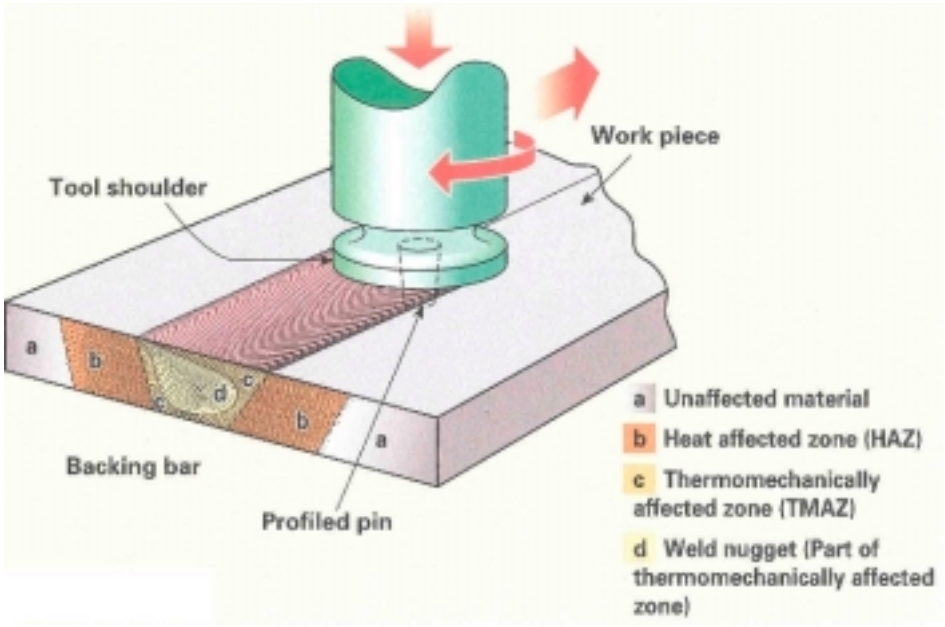

Figure 5. The principle of FSW and major weld zone regions.

Frictional heat is generated by the rubbing action of the tool against the copper plates which creates a softened region at plate interface. As the tool progresses along the interface, hot softened copper is forced from the front to the back of tool. Essentially the weld interface is hot forged and consolidated creating an atomic bonded joint.

Initially SKB commissioned TWI to establish the feasibility of FSW for copper and then to progressively develop the process towards welding bases to 50mm thick copper canisters. An important stage in the development programme was a demonstration that 50mm thick copper could be successfully friction stir welded as shown in Fig. 6.

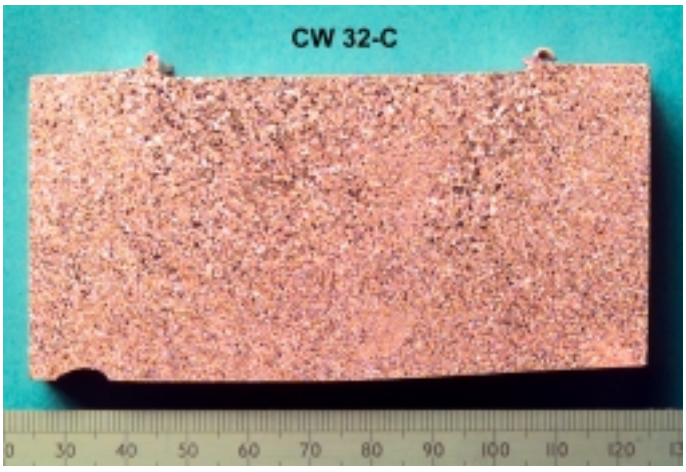

Figure 6. A transverse metallurgical section through a 50mm thick copper stir weld.

This achievement provided sufficient confidence for SKB to commission TWI to design and manufacture of a full size experimental canister to base FSW machine. The machine is designed so that the canister is gripped vertically in a radial clamping system which can be

rotated up to a welding speed of 150mm/min. A weld is made using hydraulic actuators to force the rotating FSW tool into the joint between the canister and base. In order to prevent the base and canister from separating when the FSW tool passes along the weld interface, they are held together by an additional hydraulic clamping system. The rapid development of a welding procedure that generates good quality welds has been greatly assisted by a sensitive monitoring system that records temperatures, forces and mechanical movements.

In November 2000 the first 3.3m long complete circumferential canister to base weld was made as shown in Fig. 7.

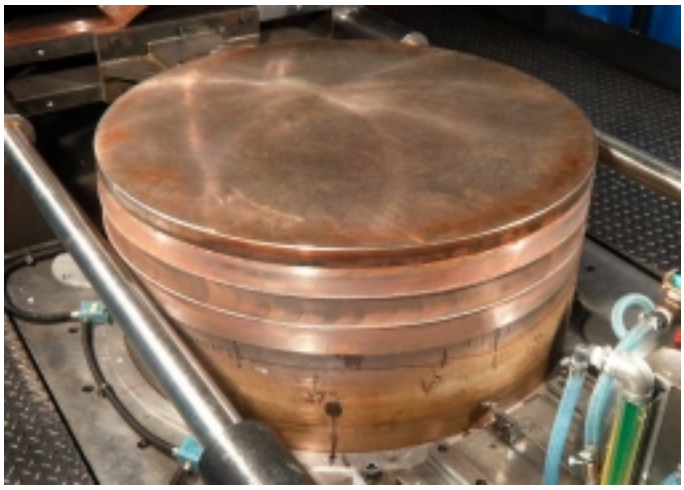

Figure 7. A complete circumferential friction stir welded canister.

This breakthrough was assisted greatly by the parallel development of FSW tools that were designed to withstand the temperature and pressure generated during the weld cycle. Development of welding procedure continues at TWI to ensure that the FSW process can be used in pre-production canister welding trials as quickly as possible.

6. Summary.

SKB and TWI have explored the potential of both RPEBW and FSW for sealing copper nuclear waste storage canisters. Both processes have been demonstrated as being capable of producing good quality base/lid to canister welds on full size canisters. Continued evaluation of these techniques will continue using pilot production equipment at SKB's Canister Laboratory, where production welding procedure will be established.

In 2004 the preferred canister sealing method will be identified for production use in the Encapsulation Plant and Canister Factory.

ULTRASONIC IMAGING AND EVALUATION OF ELECTRON BEAM WELDS IN COPPER CANISTERS

Tadeusz Stepinski and Ping Wu
Uppsala University, Department of Materials Science, Signals and Systems,
Box 528, S-751 20 Uppsala, Sweden

ABSTRACT

An EB weld, similarly to other types of welds, is characterized by a layered structure consisting of a host material zone (HMZ), a heat-affected zone (HAZ), and a fusion zone (FZ). A high quality ultrasonic image with well pronounced both HAZ and FZ is required for the evaluation of EB weld. Since the size of grains in the HMZ, HAZ and FZ differs considerably (usually grains are fine in the HMZ, get bigger in the HAZ, and become coarse in the FZ), the scattering patterns (associated with imaging contrast) in the zones are different. Since the scattering patterns are frequency-dependent, the HAZ and the FZ cannot be satisfactorily imaged simultaneously using a single band-limited ultrasonic transducer, which is common in NDE. Our aim, presented in this paper was obtaining a satisfactory imaging of the structure and flaws located both in the HAZ and FZ of an EB weld simultaneously. The idea consists in using a pair of transducers with different center frequencies. An experimental study has been conducted in which focused transducers were used to find appropriate frequency ranges best suitable for the imaging of different zones of the EB weld. The results have demonstrated that for the EB welds in our specimens an ultrasound with a frequency range of 4-5 MHz was suitable for the HAZ while satisfactory images of the FZ could be obtained using a frequency range of 2-3 MHz. A pair of transducers with the above frequency ranges yielded clear images of the layered structure of an EB weld. This means that the HAZ and FZ could be clearly distinguished using those transducers enabling estimation of the weld parameters, e.g., the thickness of the HAZ and HZ, and the grain sizes in different zones.

INTRODUCTION

Electron beam (EB) welding is a fusion welding process using energy of a beam of high-speed electrons dissipated in the metal to weld metals. An EB weld, in general, consists of a fusion zone (FZ) and a heat-affected zone (HAZ) (see Figure 1). The microstructure (e.g., grain size and elasticity) in the fusion and heat-affected zones is different, depending on the amount of heat developed. Therefore, a copper canister with an EB weld is a layered medium in which the EB weld is an embedded multiple layer. This multiple layered structure can be investigated using ultrasonic imaging when an EB weld is inspected using an ultrasonic beam perpendicular to the weld plain (see Figure 1). The ultrasonic grain noise patterns in the FZ, HAZ and the host material appear to be different, that is, grains are fine in the HMZ, get bigger in the HAZ, and become coarse in the FZ. It is the difference of grain sizes in the HMZ, HAZ and FZ that makes the scattering pattern different in each zone, and a different scattering pattern results in different imaging contrast. Since the scattering pattern is frequency-dependent, and ultrasonic transducers that are commonly used in ultrasonic NDE are band-limited, the HAZ and the FZ are difficult to be satisfactorily imaged simultaneously with one transducer. In the present work we present an experimental study with that has made possible satisfactory imaging of both the HAZ and FZ of an EB weld simultaneously.

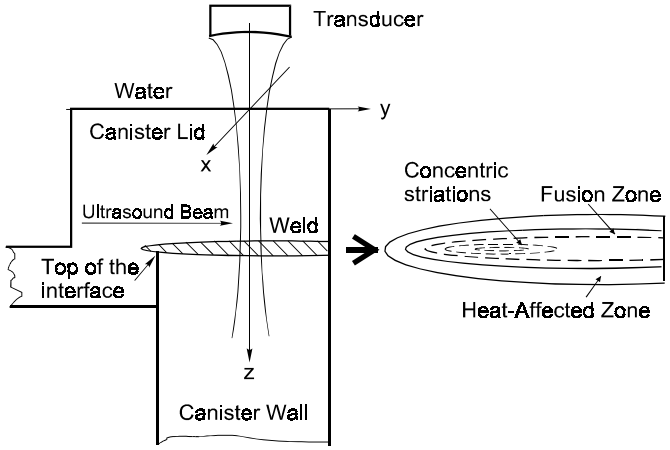

Figure 1. Schematic of EB weld structure and of ultrasonic inspection of the EB weld.

EXPERIMENTAL SETUP AND MEASUREMENTS

The experimental setup used for this study, consisting of a two-element annular transducer array with the ultrasonic array system ALLIN used in the experiments is shown in Figure 2(a). The copper block inspected was a section of an EB weld in copper canister referred to as CAN 1. The CAN 1 included 9 pairs of drilled holes, #1 to #9 drilled in the EB weld, and #10 to #18 in the parent material (see Figure 2(b)).

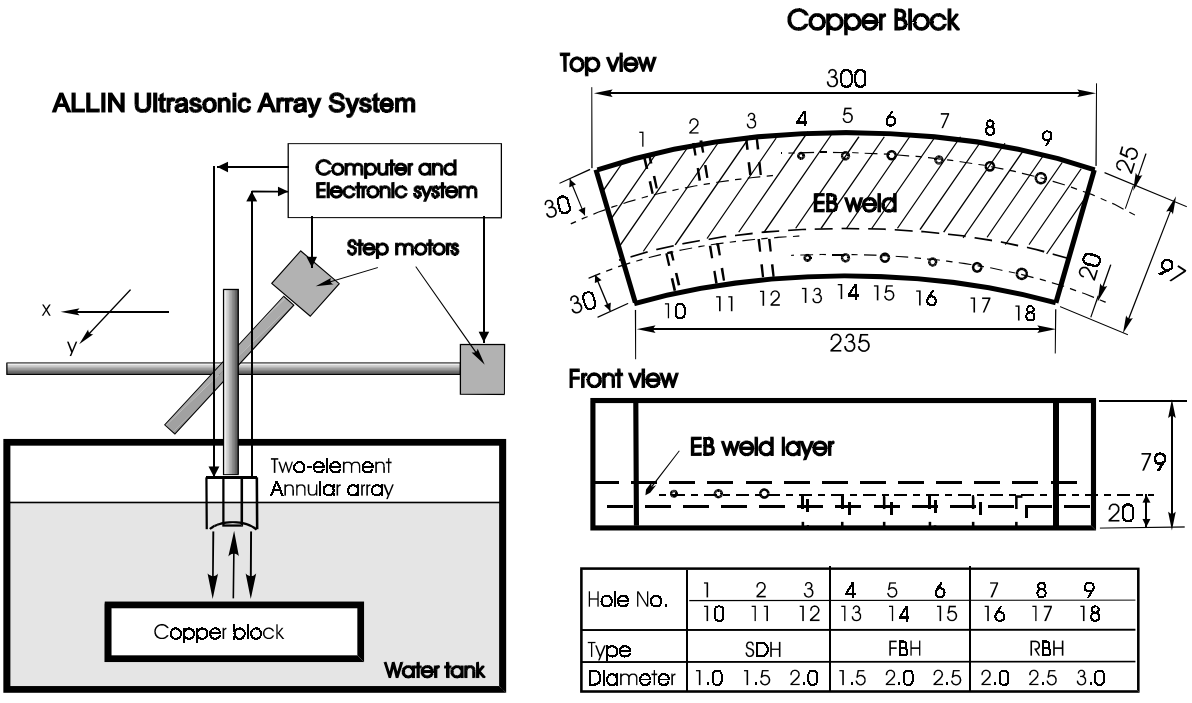

Hole No.	1	2	3	4	5	6	7	8	9
	10	11	12	13	14	15	16	17	18
Type	SDH			FBH			RBH		
Diameter	1.0	1.5	2.0	1.5	2.0	2.5	2.0	2.5	3.0

(a) (b)

Figure 2. (a) Experimental setup, and (b) the inspected copper block CAN 1.

The transducer used has two spherically concentric elements with radius of curvature of 210 mm. The inner element is circular with a 20-mm diameter, and has a 4.83-MHz center frequency with a 73% bandwidth. The outer element is annular with an approximate 20-mm inner diameter and a 38-mm outer diameter, and has a 2.26-MHz center frequency with a 69% bandwidth. The horizontal and vertical directions are assumed to be the *x* and *y*

directions, respectively. The region of interest selected and mechanically scanned is an area including all 9 pairs of holes located both within and outside the EB weld zone, respectively (see Figure 2(a)). During the inspection, carried out using a mechanical XY scanner a 3-dimentional ultrasonic data was acquired. From these data C-scans were extracted by taking the absolute maximum values of echoes in the properly selected time gates, and the B- and A-scans of interest can be located from the C-scans. Note that the B- and A-scans in this report are displayed in such a way that the vertical axis is y (one scanning direction) and the horizontal is z (the depth). This implies that the transducers are positioned on the left-hand side of images. For examining ultrasonic scattering from EB weld we used the two-element annular array transducer, and also the third one, Panametrics V315. The latter one had nominal center frequency of 10 MHz, but a measured center frequency of 8.65 MHz and the measured –6 dB bandwidth of 82%.

IMAGING EB WELDS

As a reference to ultrasonic inspection a radiographic inspection of the CAN 1 has been performed. Below we will present and compare results of both inspections.

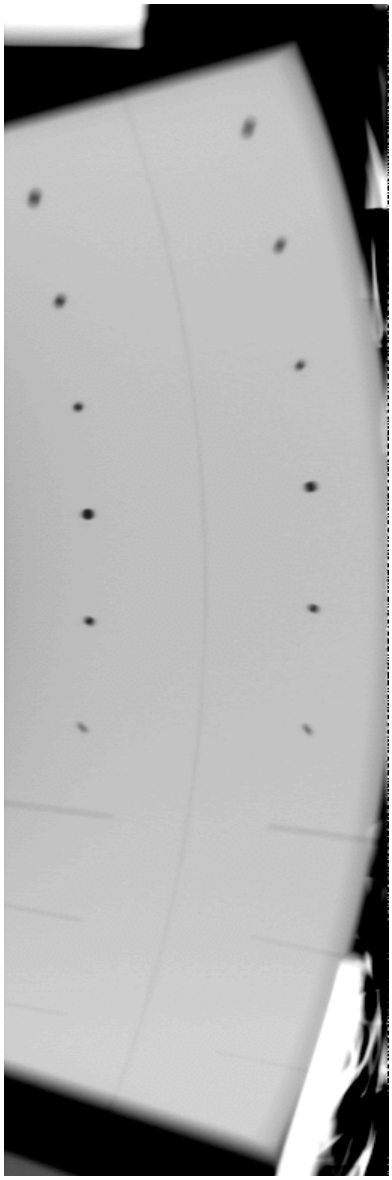

The radiograph of the EB weld in copper block CAN 1 (top view) is shown Fig. 3. The contrast and brightness of the image have been adjusted to get the best illustration of the artificial defects (the side- and bottom-drilled holes). From the images all nine pairs of holes can be seen. It is easy to notice that the bottom-drilled holes (FBH #4-6, #13-15, and RBH #7-9, #16-18) are characterized by high contrast while the SDHs by a low contrast. The reason for that is simple, the contrast observed at the radiographic image increases with void size in the beam direction. We can also see an arc going in the middle, which is the interface between the canister wall and the lid. However, only a little information on the structure of EB welds can be captured, and the welded and non-welded zones can not be distinguished from the radiograph.

Ultrasonic C-scans provide an overall, top view of an inspected sample, similar to that provided by the radiograph. The ultrasonic images of CAN 1 obtained using the 2.26-MHz transducer in pulse-echo mode are shown in Fig. 4. The C-scans in the figure were obtained using the time gates set at different time (or depth) intervals. An appropriate gate adjustment for extracting C-scans is very important for the effective exploitation of information characterizing the inspected material, especially for EB welds that are layered media with large attenuation.

Figure 3. Radiograph of the CAN1, top view.

Quite a detailed investigation of this problem has been done in our earlier work, cf. [1].
The C-scan shown in panel (a) of the Fig. 4 is extracted using the gate that covers the fusion zone (FZ) of the EB weld. Since the SDHs and the tops of the bottom-drilled holes are located at 60 mm beneath the canister's surface, the depth where the FZ of the weld is located, the images of all the holes in the specimen are well pronounced in this C-scan. The C-scan in panel (b), showing the interface between the wall and the lid, was constructed with the gate set deeper than the gate in panel (a) which means that the gate covered the interface between the back heat-affected zone (HAZ) and the host material. The interface might not be seen if the gate was not set properly because the scattering from the interface, although being stronger in the properly gated layer, can be weaker than the scattering from the grains in the FZ.

The C-scans presented in the panels (a) and (b) in Fig. 4 jointly provide information on the weld that is similar to that obtained from the radiograph (Fig. 3); that is, the nine pairs of the holes and the wall/lid interface are well pronounced. The resolution of the 2.26-MHz transducer is comparable with that in the radiograph. From ultrasonic images the information on the structure of EB welds can be captured; for example, the layered structure and the grain difference in the layers are distinguishable. This is an advantage of the ultrasonic technique over the radiography. At the same time it is a disadvantage since scattering from the structure appears as grain noise that often masks flaws and hence makes the flaws more difficult to be detected. Unlike in the radiographs, mapping of the SDHs in the ultrasonic images at the edge of the block is not perfect. This is because the block edge is inspected using only a part of the transducer aperture.

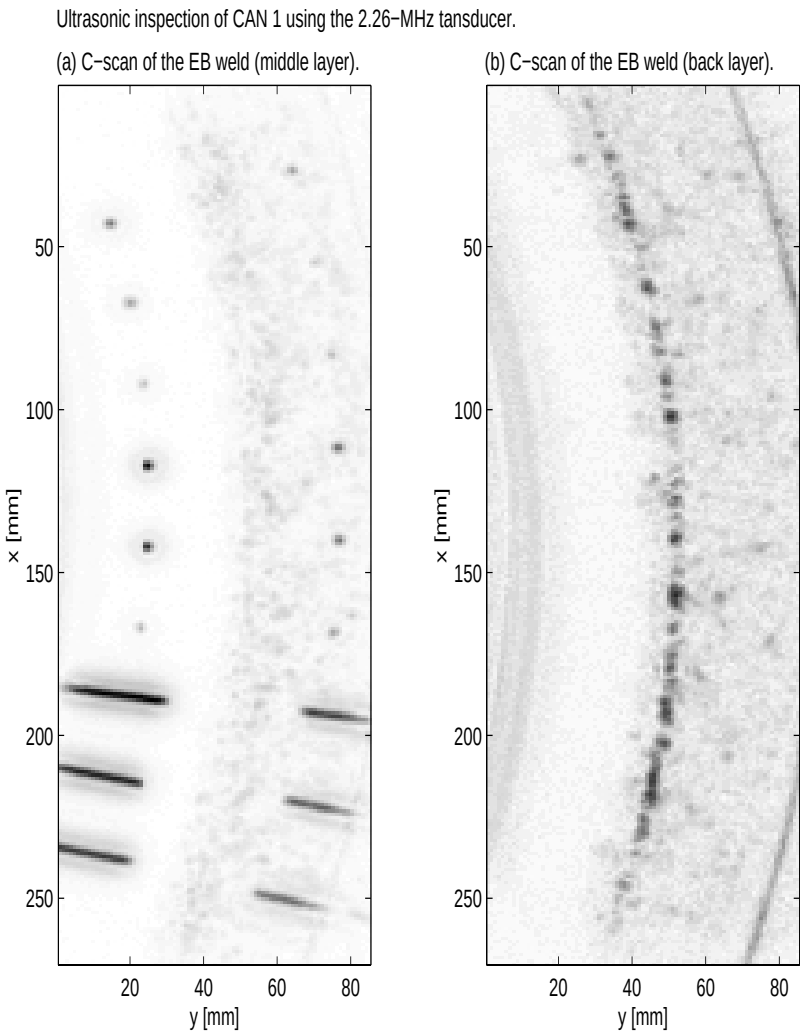

Figure 4. Ultrasonic images of the copper block CAN 1 obtained using the 2.26 MHz transducer. C-scans of the CAN 1 with the gates located over (a) the middle layer (the FZ) and (b) the back layer (the back HAZ), respectively.

ULTRASONIC SCATTERING OF EB WELDS

As we have seen, C-scans yield an overall, top view of an EB weld and the dynamic range of scattered echoes. To examine the structure of an EB weld, the cross-sectional view that is shown in B-scan is helpful. To the purpose, we used the three transducers with center frequencies of 2.26, 4.83 and 8.65 MHz.

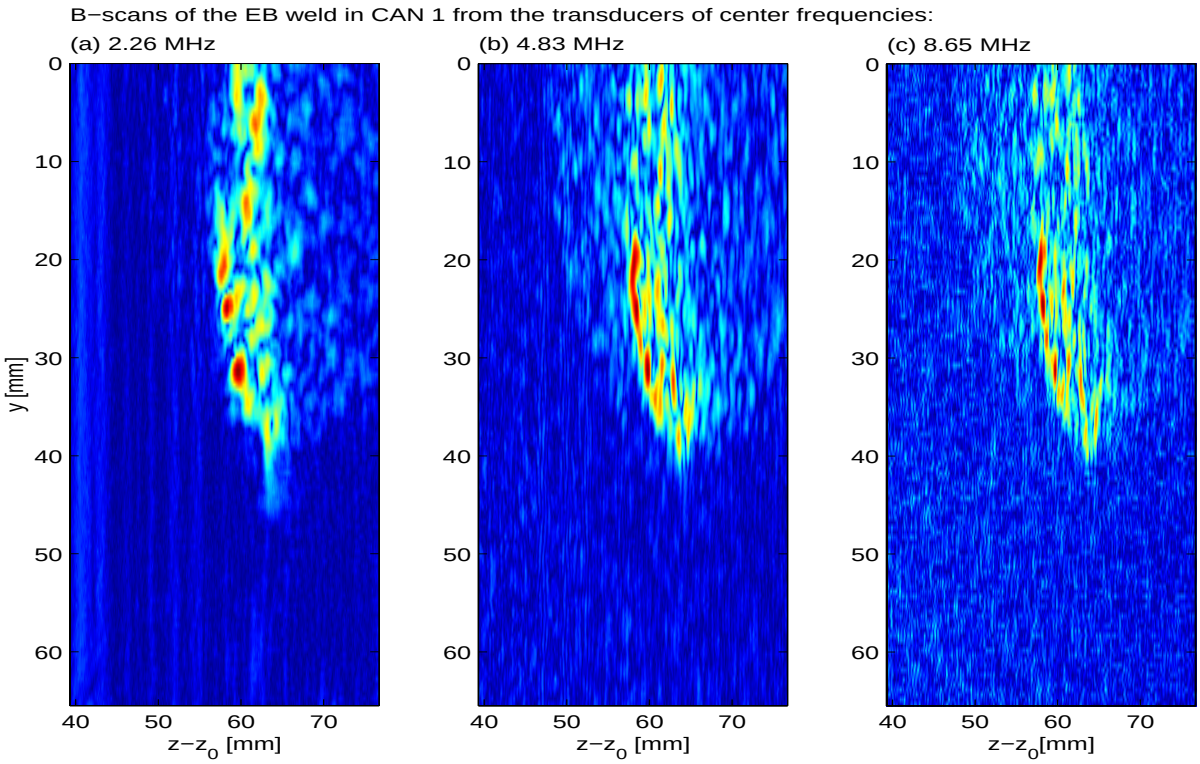

Figure 6. B-scans of the EB weld in CAN 1 form the transducers with three different center frequencies: (a) 2.26 MHz, (b) 4-83 MHz, and (c) 8.65 MHz. Here z_0 is the water path length. The scans are located at x=6 mm in Figures 3 (b) and 4 (b).

The first two transducers are the separate elements of the two-element annular array transducer used in the previous section, and the third one used is Panametrics V315 with a measured center frequency of 8.65 MHz. The transducers were used with the ALLIN system in the similar way as shown in Figure 2. The B-scans from those three transducers are shown in Figure 6(a), (b) and (c), respectively. Vertical axis in Figure 6 is the scanning position y and the horizontal axis is z-z_0 (where z_0 is the path length of the water layer), the depth in the copper block. Note that logarithmic scale of the signal envelope in these images used to highlight the weak scattering from the HAZ.

From these B-scans we can examine the cross-section of the EB weld. The tip of the weld is located around y=42 mm, z-z_0=60. In each image a strip-like strong echo zone is seen that indicates the FZ within the region of y=0~42 mm, z-z_0=56~64 mm. In the B-scan from the 2.26-MHz transducer the HAZ is very difficult to see. But the HAZ is easy to see in the B-scan from the 4.83-MHz transducer as well as the 8.65-MHz transducers (however, for the 8.65-MHz transducers the grain noise from the host material is more apparent and the electronic noise becomes larger as well). The reason for this is that the fine grains (in the

HAZ) result in less scattering to the low frequency ultrasound than to the higher frequency one. In other words, the higher frequency ultrasound is more sensitive to fine grains. From Figure 6(b), the thickness of the HAZ can be measured to be around 8 mm (from 48~56 mm in the *z* direction) in front of the EB weld. Therefore, to inspect the HAZ of an EB weld, a transducer with higher frequency, e.g., 5 MHz, may be a good choice (if the EB welding process is made under normal conditions). To inspect the FZ, the transducer with lower frequency, e.g., 2~3 MHz (from the present and the early research [1]), can be a better choice. Combination of the inspections in the two frequency bands will give us more information on EB welds.

CONCLUSIONS

An ultrasonic imaging of EB weld in copper canister has been conducted using three transducers with different center frequencies. The results have demonstrated that ultrasound is not only capable of detecting small artificial defects (holes) in the weld zone but it also can provide an useful information on the internal weld structure.

For the EB welds in our specimens an ultrasound with a frequency range of 4-5 MHz was suitable for the HAZ while satisfactory images of the FZ could be obtained using a frequency range of 2-3 MHz. A pair of transducers with the above frequency ranges yielded clear images of the layered structure of an EB weld, so that the HAZ and FZ could be clearly distinguished and the thickness of the HAZ and HZ are possibly measured.

ACKNOWLEDGEMEMT

This work was supported by the Swedish Nuclear Fuel and Waste Management Co. (SKB).

REFERENCES

1. P. Wu, Fredrik Lingvall, and T. Stepinski, *Inspection of Copper Canisters for Spent Nuclear Fuel by Means of Ultrasonic Array System – Electron Beam Evaluation, Modeling and Materials Characterization*, SKB Technical Report TR-99-43, December 1999.